Gabriel Jordão Guedes Nascimento

Modeling Photoluminescence Dynamics in NV Ensembles with Charge Conversion Effects

Rio de Janeiro
2026

Gabriel Jordão Guedes Nascimento

Modeling Photoluminescence Dynamics in NV Ensembles with Charge Conversion Effects

Dissertation submitted to the Graduate Program in Physics in partial fulfillment of the requirements for the degree of Master of Science.

Advisor: Alexandre Martins de Souza

Centro Brasileiro de Pesquisas Físicas
MSc Program

Rio de Janeiro
2026

"MODELING PHOTOLUMINESCENTE DYNAMICS IN NV ENSEMBLES WITH CHARGE CONVERSION EFFECTS"

GABRIEL JORDÃO GUEDES NASCIMENTO

Dissertação de Mestrado em Física apresentada no Centro Brasileiro de Pesquisas Físicas do Ministério da Ciência Tecnologia e Inovação. Fazendo parte da banca examinadora os seguintes professores:

Alexandre Martins de Souza - Orientador/CBPF

gov.br Documento assinado digitalmente
SERGIO RICARDO MUNIZ
Data: 19/06/2026 10:24:23-0300
Verifique em https://validar.iti.gov.br

Sergio Ricardo Muniz – IFSC/USP

gov.br Documento assinado digitalmente
ANDERSON MONTEIRO AMARAL
Data: 19/06/2026 12:00:26-0300
Verifique em https://validar.iti.gov.br

Anderson Monteiro Amaral – UFPE

Rio de Janeiro, 22 de maio de 2026.

Acknowledgements

Agradeço primeiramente ao meu pai, Ubirajara Guedes Nascimento, que, sem seu apoio incondicional esse trabalho não existiria, e provavelmente nem estaria seguindo a carreira na Física. Te amo e obrigado por tudo. Dedico também esse trabalho à minha mãe, Marlicea Jordão da Silva, que mesmo de longe fez de todo o possível para me ajudar.

Também agradeço ao meu orientador Alexandre, pela paciência e pelo encaminhamento do trabalho, sempre estando disposto a ajudar em qualquer detalhe que seja. Um muito obrigado a Carmem que contribuiu substancialmente com discussões e com os experimentos. Agradeço também ao CBPF, minha casa por todos esses anos. Com toda sua estrutura, pude aprender e realizar experimentos, com conforto e segurança chegando até dormir na instituições por algumas ocasiões. Um ambiente que não tenho dúvidas serve como referência mundial.

Ao programa de fomento CAPES, às instituições públicas de ensino, UFRJ, CEFET/RJ, às políticas afirmativas, meu muito obrigado. Não estaria aqui sem esses programas e instituições na minha vida. Agradeço ousadamente falando por todo o país. Torço para que a ciência seja cada vez mais valorizada e espero que minha vida testemunhe a favor do valor das políticas públicas de ensino.

Um agradecimento também a todos meus amigos, que tornaram essa caminhada mais leve. Aos amigos da Grande Rede de Apoio, meus compadres Babi e Mei, Inaê e sua contraparte Enéas, Matheus viciado, e o Cunha também, Dona Dani Racossi; também aos amigos do New Era, Farah, Cat, Pinhel, Nilson, Ian, Luan, Renan e em especial ao primeiro pai do grupo, Carvas, que sem ele não viraria tantas noites ouvindo música no spotify. Agradeço aos amigos do Rock, Macook, Berg e Galo. Vocês são demais. Sempre acompanhando nos shows e me permitindo fazer a coisa que mais gosto: falar de música. Dedico também um grande abraço aos meus amigos de trabalho: Luiza, Marcela, Marcus, JP, Mari, Laís, Alan e todos os demais que compartilham momentos dentro e fora do CBPF.

Um agradecimento especial à Karina, que me ajudou de diversas formas durante a reta final do mestrado. Já trabahei com seu computador, recebi carona, já preparou comida e definitivamente compartilhamos momentos essenciais para que eu conseguisse superar a dificultade que é fazer uma pós-graduação em física.

Finalmente, dedico também esse trabalho a todos os artistas que admiro, pois sem suas artes a minha vida com certeza teria muito menos sentido e faltaria motivação para enfrentar o cotidiano. Mesmo que provavelmente essa dedicatória jamais chegue a vocês, agradeço profundamente aos artistas: Armin Van Buuren (sempre trilha sonora dos estudos),Summoning, Death, Hällas, Moonlight Sorcery,Velho, Midnight Odyssey, Twin Tribes, She Past Away e a todos que já tenham apresentado sua arte para o mundo.

"All we have to decide is what to do with the time that is given us."

— J. R. R. Tolkien

Abstract

In this work, we present a simulation framework to describe the electronic dynamics of nitrogen-vacancy (NV) centers in diamond.

The model is formulated within a matrix-based approach, where the system evolution is governed by transition-rate matrices and modulated by a stretched-exponential term. One matrix describes the dynamics under continuous optical excitation, while a second matrix accounts for the electronic evolution in the absence of laser illumination (dark conditions). The inclusion of the stretched-exponential contribution captures slow charge-conversion processes, leading to variations in the NV^- population, which we attribute to two-photon absorption processes involving NV^0 in our sample.

Our model is developed from the standard rate-equation formalism widely used in the literature. We first analyze how this baseline model reproduces key experimental observables, particularly the photoluminescence (PL) response. We then extend the model by incorporating additional physical mechanisms, such as charge conversion, and apply the formalism to characterize a diamond sample available in our laboratory.

The methodology developed here provides a systematic and reproducible protocol for the characterization of NV-center ensembles with varying defect environments and material properties, extending beyond the specific sample investigated in this work.

Keywords: NV Centers; NV Center characterization; NV Center simulation.

Resumo

Neste trabalho, apresentamos uma estrutura de simulação para descrever a dinâmica eletrônica de centros de vacância de nitrogênio (NV) em diamante.

O modelo é formulado dentro de uma abordagem matricial, na qual a evolução do sistema é governada por matrizes de taxas de transição e modulada por um termo de exponencial esticada. Uma matriz descreve a dinâmica sob excitação óptica contínua, enquanto uma segunda matriz representa a evolução eletrônica na ausência de iluminação (condições de escuro). A inclusão do termo de exponencial esticada captura processos lentos de conversão de carga, levando a variações na população de NV^-, que atribuímos a processos de absorção de dois fótons envolvendo NV^0 em nossa amostra.

O modelo é baseado em um formalismo de equações de taxa amplamente utilizado na literatura. Inicialmente, analisamos como esse modelo base reproduz observáveis experimentais fundamentais, em particular a resposta de fotoluminescência (PL). Em seguida, estendemos o modelo incorporando mecanismos físicos adicionais, como conversão de carga, e aplicamos o formalismo para caracterizar uma amostra de diamante disponível em nosso laboratório.

A metodologia desenvolvida aqui fornece um protocolo sistemático e reprodutível para a caracterização de ensembles de centros NV com diferentes ambientes de defeitos e propriedades do material, indo além da amostra específica investigada neste trabalho.
Palavras-chave: Centros NV; Caracterização de centros NV; Simulação de centros NV.

Contents

List of Figures

List of Tables

1 Introduction

A Nitrogen-Vacancy (NV) center is a point defect in the diamond lattice, corresponding to the replacement of one carbon atom by nitrogen and the absence of a neighboring carbon atom. This system emits **photoluminescence (PL)** and PL measurements give information about physical properties of the NV's local environment, such as temperature, magnetic and electric field (Rembold *et al.*, 2020). There are two main types of NV centers (Doherty *et al.*, 2013): NV^0, whose ground state has spin-1/2 character, and NV^-, a spin-1 system. Their electronic energy structures make these two systems fundamentally different, with the latter being of particular interest in many areas of quantum information due to its favorable optical properties at room temperature.

The broad range of applications of the NV center arise from its spin and optical properties, which will be discussed in detail later (chapter 2). Under optical excitation, the NV electronic dynamics enable efficient spin polarization into the $m_s = 0$ ground-state sublevel. The $m_s = 0$ and $m_s = \pm 1$ energy levels are separated by a well-defined zero-field splitting in the microwave frequency range, enabling coherent spin manipulation of the sublevels through resonant microwave pulse protocols. The PL intensity and decay depend on the population distribution among the ground-state spin sublevels, enabling optical readout of the NV spin state. External magnetic fields lift the degeneracy of the $m_s = \pm 1$ levels via the Zeeman effect. This shift can be detected using **Optically Detected Magnetic Resonance (ODMR)** and gives quantitative information about the external magnetic field, hence, NV are mainly employed as magnetic sensors.

The study of NV energy levels and electronic dynamics is important for developing applications and for understanding the processes that enable quantitative sensing, including how magnetic fields and temperature affect the system and how these effects can be measured.

Single NVs and an ensemble of NVs can be used, depending on the applications as shown in (Taylor *et al.*, 2008). The author discusses first a single NV spin confined to a nanoscale volume that can detect magnetic field generated by the precession of individual nuclear spins. As a second application, diamond samples with a high density of NV centers can be used to sense fields created by remote objects with ultra-high sensitivity. The possibility of operation at room temperature, and the biocompatibility of diamond make the NV useful as well in biological applications, introduced into living systems, such as single cells (Rondin *et al.*, 2014).

On the other hand, zero-field splitting is temperature-dependent. A variation in temperature changes the energy difference between the $m_s = 0$ and $m_s = \pm 1$ levels, and therefore a single NV is capable of detecting small variations in temperature with reported sensitivities reaching the millikelvin range under optimized conditions and length scales of

a few nanometers (Neumann *et al.*, 2013).

Another important process within the context of NV electronic dynamics is charge photoconversion. Since charge dynamics directly affect the observed photoluminescence signal, understanding these processes allows the accurate modeling of NV ensembles. Ionization in high density NV ensembles ($NV^- \rightarrow NV^0$) (Giri *et al.*, 2018) and the back-conversion ($NV^0 \rightarrow NV^-$) on single NV (Beha *et al.*, 2012) have been reported, and studies indicate that both processes are mediated by two photons. Charge conversion makes possible a non-optical spin state readout (Shields *et al.*, 2014) that shows advantages in spin detection sensibility over traditional ODMR techniques (Bourgeois; Gulka; Nesladek, 2020).

Although the fundamental properties of the NV center are well established, practical characterization of real diamond samples remains a challenge, particularly in high-density NV ensembles where the interplay between spin polarization, optical pumping, charge photoconversion NV-NV interaction and other bulk phenomena are more impactfull.

Developing a model capable of quantitatively reproducing experimental observations and extracting physically meaningful parameters from them helps reliable and reproducible sample characterization, predicting the outcome of NV-based experiments and potential applications of the specific sample based on its characteristics.

The model developed in this work is able to reproduce the experimental photoluminescence dynamics observed in a specific diamond sample and to provide consistent effective transition rates associated with spin relaxation and charge conversion processes. Further validation across different experimental configurations constitutes a natural extension of this approach, which may help enable the use of samples characterized by the models in the applications cited above.

In this work, the ionization process ($NV^- \rightarrow NV^0$) and the back-conversion ($NV^0 \rightarrow NV^-$) are modeled as distinct dynamical channels. This explicit separation provides a clearer interpretation of how photoluminescence varies over time in NV ensembles and enables direct extraction of effective rates from experimental data.

In **chapter 2**, the properties of the NV center structure, electronic dynamics, and charge conversion that are essential for the full evaluation of this work are discussed. An introductory model that simulates the electronic dynamics in an optical cycle is introduced in **chapter 3**, together with the relation between the PL curve of a dark-time experiment and the matrices that compose the model. The details of the experiments performed in the laboratory are presented in **chapter 4**. The model expansion based on the experimental data is described in **chapter 5**. In **chapter 6**, it is shown how the simulation reproduces the experimental data, followed by a discussion of the physical parameters involved. Finally, an evaluation of our model, as well as suggestions for experiments and insights for future work are presented in **chapter 7**.

2 The Nitrogen-Vacancy Defect

2.1 Physical description

Diamond is a 3D crystalline form of carbon **(C)**, in which the atoms are arranged in a structure that can be described as two interpenetrating face-centered cubic **(FCC)** lattices displaced along the body diagonal. Numerous point and extended defects have been identified in diamond, and more than one hundred of them are optically active, naturally leading to a physical classification based on the properties that emerge due to these defects. Some of the classifications will be summarized here and more details can be found in (Zaitsev, 2001).

In **type-I** diamonds, nitrogen-related defects are present at concentrations high enough to be detected through optical absorption or **Electron Paramagnetic Resonance (EPR)**, and 98% of natural diamonds can be classified as type-I. A **type-Ia** diamond does not show absorption due to single substitutional nitrogen atoms and these impurities tend to aggregate, creating a nonparamagnetic profile in EPR spectroscopy. In contrast, if the dominating defects are paramagnetic single substitutional nitrogen, the diamond is classified as **type-Ib**. If a vacancy forms adjacent to such a substitutional nitrogen atom, a nitrogen-vacancy center may be created. **Type-II** diamonds do not show optical absorption due to nitrogen defects nor a paramagnetic profile, being sub-classified based on absorption dominated by other defects: **Type-IIa** do not show optical absorption by boron whereas **type-IIb** diamonds do show optical absorption signatures related to boron impurities, which act as acceptors and give the diamond p-type semiconducting properties.

Two main approaches are commonly used for the fabrication of NV centers: **Ion Implantation** and **Chemical Vapor Deposition (CVD)**. In the first method, high-energy nitrogen ions are accelerated and implanted into a pure diamond (usually **type IIa**) crystal, creating lattice damage and vacancy distributions along the ion trajectories. After this, the diamond goes through an **Annealing** step, with temperatures of 800°C to 1200°C, allowing the vacancies to move around the lattice and become trapped next to a nitrogen. This technique allows for high spatial control of the concentration of NVs in the diamond sample(Pezzagna *et al.*, 2010).

Alternatively, NV centers can be incorporated during diamond growth by **(CVD)**, in which NVs are created while the diamond is growing, with small doses of N_2 introduced in the chamber during the growth process. Naturally, vacancies generated during growth can become adjacent to substitutional nitrogen atoms, leading to in-situ NV formation and resulting in samples with less structural damage compared to ion implantation (Balasubramanian *et al.*, 2009).

Depending on its electronic configuration, the Nitrogen-Vacancy defect can be positively

charged (NV^+), neutral (NV^0) or negatively charged (NV^-). The symmetry of the NV center is determined by its atomic configuration thus being independent of its charge state. The defect belongs to the C_{3v} point group, characterized by a threefold rotational axis along one of the $\langle 111 \rangle$ crystallographic directions and three vertical reflection planes (Figure 1). The principal symmetry axis coincides with the N–V bond direction, and defines a natural quantization axis for the electronic spin. This symmetry also governs the classification of the electronic states into representations (A_1, A_2, and E) and determines transition selection rules (Gilardoni, 2021).

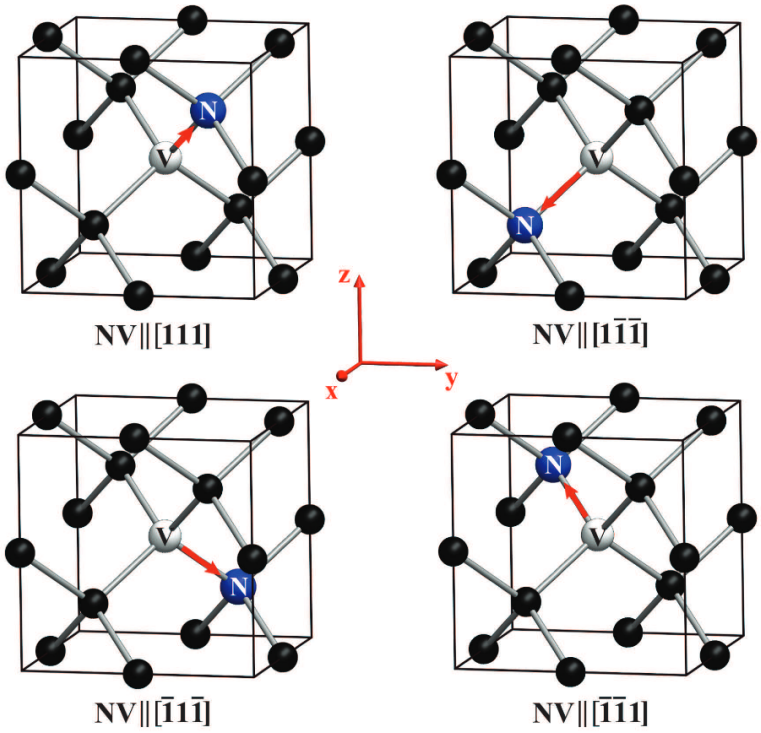

Source: (Pham *et al.*, 2012)

Figure 1 – The NV symmetry axis lies along a body diagonal of the cubic diamond lattice represented by the Miller indices [111], and together with the three other symmetry-equivalent orientations, these directions form the $\langle 111 \rangle$ family. The red arrows indicate the quantization z-axis associated with each orientation.

2.2 Negatively charged NV

2.2.1 Electronic Structure

The negatively charged NV center (NV^-) exhibits a strong optical transition at 1.945 eV (637 nm) (Figure 2), corresponding to the **zero-phonon line (ZPL)** of the ${}^3A_2 \leftrightarrow {}^3E$ transition, which is followed by prominent vibronic side bands, both in absorption and emission spectra. The electronic ground state of the NV^- is a spin-triplet state ($S = 1$), composed by six electrons occupying molecular orbitals (MO) formed by the dangling bonds of the nitrogen atom and the three adjacent carbon atoms, with one additional electron

from a donor in the lattice. The zero-field splitting is a result of spin-spin interaction that lifts the degeneracy of the $m_S = 0$ and $m_S = \pm 1$ sublevels, with parameters: $D \approx 2.87$ GHz and $E \approx 0$ (Doherty *et al.*, 2013). These parameters will appear in the effective Hamiltonian for the ground state.

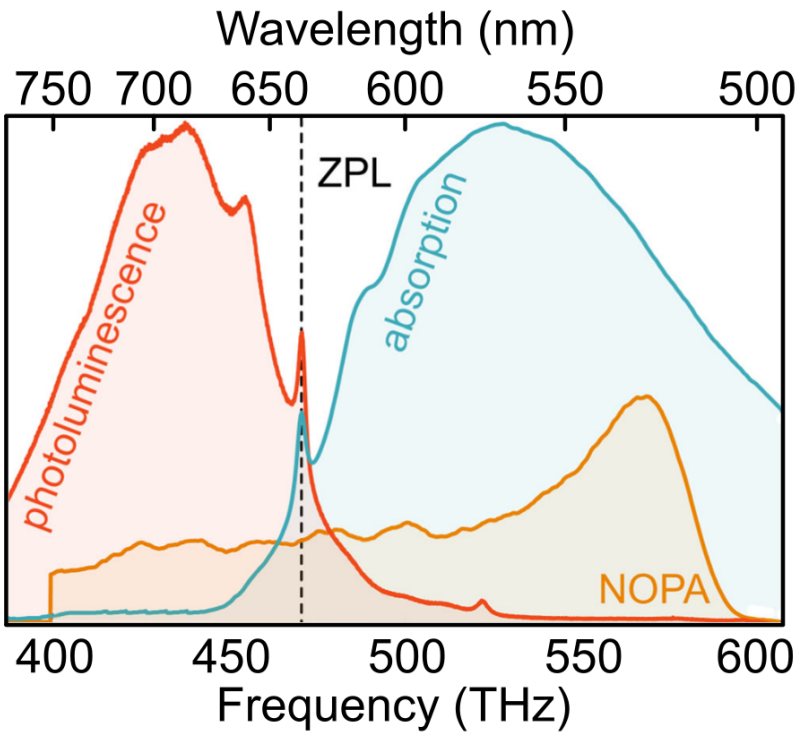

Source: (Carbery *et al.*, 2024)

Figure 2 – NV^- emission and absorption curves. Red line is the NV emission (PL). Blue line is the absorption and orange line is the laser spectrum. Dotted vertical line is the ZPL at 470.3 THz (637.4 nm)

2.2.2 Ground-State Hamiltonian

The electronic ground state of the NV^- center is a spin-triplet state ($S = 1$), whose dynamics can be described by an effective spin Hamiltonian. In the absence of external perturbations, the dominant interaction arises from spin–spin dipolar coupling between the unpaired electrons.

This interaction splits the $m_S = 0$ level from the degenerate $m_S = \pm 1$ sublevels even in the absence of an external magnetic field, leading to an energy gap ZFS. The corresponding Hamiltonian term is written as

$$\hat{H}_{\text{ZFS}} = D\left(\hat{S}_z^2 - \frac{\hat{S}(\hat{S}+1)}{3}\right) + E(\hat{S}_x^2 - \hat{S}_y^2), \tag{2.1}$$

where $D \approx 2.87$ GHz is the axial zero-field splitting parameter and E accounts for transverse symmetry-breaking effects such as strain. The parameter D varies with

temperature and pressure, with coefficients of approximately -80 kHz/K and 1.5 kHz/bar, respectively (Rembold *et al.*, 2020).

In the ideal case of perfect symmetry, $E = 0$ and the $m_S = \pm 1$ states remain degenerate. However, lattice strain or electric fields can reduce the symmetry and induce a finite E, lifting this degeneracy.

In the presence of an external magnetic field $\mathbf{B}$ aligned to the quantization axis z (Figure 1), the Zeeman interaction must be included, yielding the effective Hamiltonian:

$$\hat{H} = \hbar D \left(\hat{S}_z^2 - \frac{\hat{S}(\hat{S}+1)}{3} \right) + \hbar E(\hat{S}_x^2 - \hat{S}_y^2) + g\mu_B \mathbf{B} \cdot \hat{\mathbf{S}}, \tag{2.2}$$

where $g \approx 2$ is the electronic Landé factor and μ_B is the Bohr magneton. There are hyperfine and spin–nuclear interaction terms in the full Hamiltonian, but they will not be considered in this work.

This Hamiltonian hints an important feature of NV^-. The parameter D lies in the microwave frequency range, so microwave radiation is used to drive transitions between the $m_S = 0$ and $m_S = \pm 1$ sublevels, fundamental for ODMR experiments and population control in the ground state, enabling coherent manipulation and optical readout of the electronic spin.

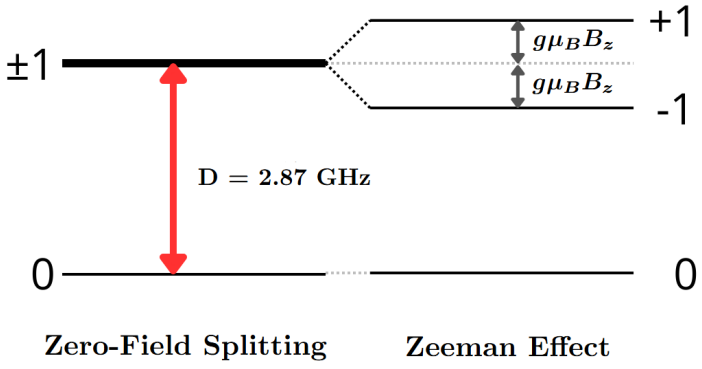

Source: By the author.

Figure 3 – Ground-state energy level in absence of magnetic field (left) and in the presence of a magnetic field (right).

2.2.3 Optical Cycle

The intrinsic electronic dynamics of the NV^- center are responsible for spin polarization and spin readout, two key features of this system. The six-level model shown in Figure 5 illustrates the main processes governing these dynamics.

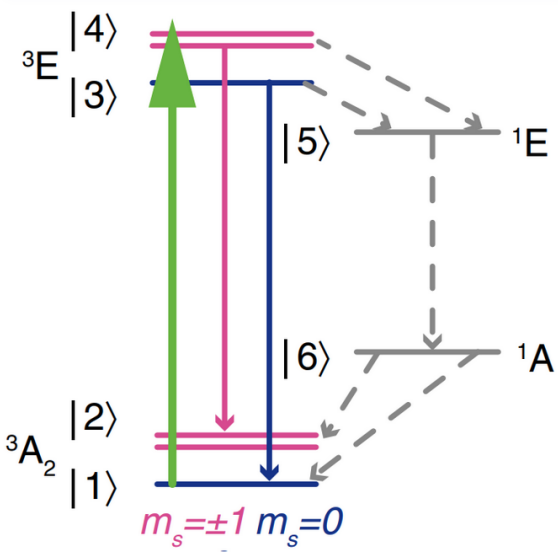

ADAPTED FROM:(Song *et al.*, 2020)

Figure 4 – Six level model of the electronic dynamics in the negatively charged NV . Solid blue and pink lines represent radiative decay. Green arrow represents non-resonant laser excitation. Gray dashed arrows represent the singlet dynamics via ISC which is predominantly non-radiative.

Under green laser excitation (typically 532 nm or 509 nm), the population from the ground state is promoted to the excited triplet state ^3E. This transition is largely spin-conserving (Robledo *et al.*, 2011). Green-light excitation is highly efficient due to the strong coupling between the NV center electronic levels and the vibronic modes of the diamond lattice. This coupling gives rise to a broad phonon sideband in the absorption spectrum (see Figure 2), extending well above the zero-phonon line at 637 nm.

Upon absorption of a photon with energy greater than the ZPL transition energy, the NV center is promoted to vibronically excited levels of the ^3E state, followed by rapid non-radiative relaxation within the excited-state manifold to its lowest vibronic level. Efficient optical excitation is typically achieved in the green spectral range (510–550 nm) (Aslam *et al.*, 2013). More details on the NV vibronic structure can be found in (Doherty *et al.*, 2013).

The phonon sideband is a broad absorption spectrum, providing a continuum of vibronic transitions that significantly enhance the absorption probability. Green-light is also sufficiently energetic to convert NV^0 dark states into NV^- increasing the PL, as discussed later in subsection 2.2.5.

Electrons in the ^3E state predominantly decay to the $^3A_2$ state by emitting a photon whose wavelenght follows Figure 2 while also preserving their spin projection, thus returning to the $^3A_2$.

However, they can also decay via a non-radiative channel, to the ^1E. This non-radiative transition from the triplet excited state to the singlet manifold is called **Inter-System Crossing**, where the electron loses energy to the lattice mediated by spin–orbit and

vibronic interactions (Penfold *et al.*, 2018). In the metastable singlet state, the transition ${}^1 \rightarrow {}^1A_1$ emits photons within infrared (IR) range around 1042 nm.

The non-radiative decay of the ${}^3E$ through the singlet state is more likely to happen for the electronic sublevels $m_s = \pm 1$ so it is responsible for the spin selectivity. After many optical cycles, the electrons in a NV ensemble are mostly populated in the $m_s = 0$ sublevel (initialization of the NV), resulting in enhanced PL. This spin-dependent PL enables optical readout of the spin state.

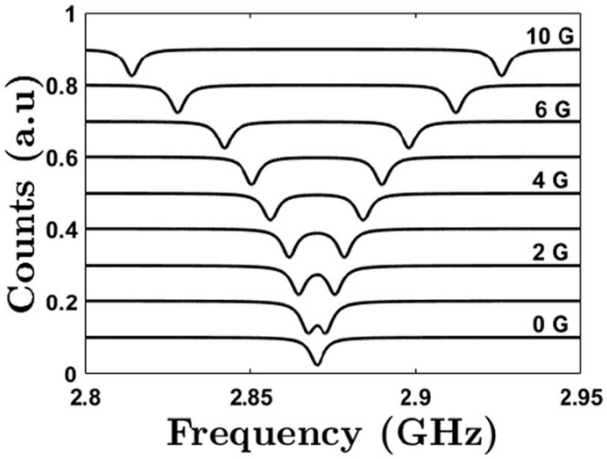

Source:(Rembold *et al.*, 2020)

Figure 5 – Simulated optically detected magnetic resonance (ODMR) spectra of the NV^- center for different magnetic field magnitudes, showing the splitting of the $m_s = \pm 1$ transitions. Photoluminescence (PL) as a function of microwave frequency.

The spin dependence of the photoluminescence, together with the zero-field splitting and the strong spin–magnetic field coupling described in subsection 2.2.2, makes the NV center a highly sensitive magnetic sensor. Once the NV center is optically initialized into the $m_s = 0$ state, a drop in PL can be observed while sweeping the microwave frequency. When the microwave frequency matches the spin transition frequency near the zero-field splitting at 2.87 GHz, population is transferred from the $m_s = 0$ sublevel to the $m_s = \pm 1$ sublevels. Upon application of a static magnetic field, the $m_s = +1$ and $m_s = -1$ are no longer degenerate, two dips appear. The Zeeman frequency splitting between these dips is given by $\Delta f = 2g\mu_B B_z$ and is proportional to the projection of the magnetic field along the NV symmetry axis, as described by Equation 2.2.

2.2.4 Spin Relaxation and Coherence Times

The performance of NV-based quantum sensing and information protocols is ultimately limited by the characteristic spin relaxation and coherence times of the ground-state triplet.

The longitudinal relaxation time T_1 describes population relaxation between spin sublevels. Physically, it corresponds to the time scale over which the system returns to thermal equilibrium after optical polarization. At room temperature, T_1 in high-purity diamond can reach the millisecond range and is primarily limited by spin–lattice interactions. The value of T_1 depends on sample size, temperature, and the concentration of impurities in the crystal. (Tetienne; Hingant, *et al.*, 2013).

The transverse relaxation time T_2 characterizes the decay of quantum coherence between superpositions of spin states caused by fluctuating interactions that dephase these states due to magnetic noise from the surrounding spin environment, including ^{13}C nuclear spins and other paramagnetic defects. In isotopically purified samples, T_2 can reach hundreds of microseconds and even approach the millisecond regime under dynamical decoupling sequences (Mizuochi *et al.*, 2009).

In ensembles, each NV has different local conditions and the expectation value of a given observable must be averaged. This averaging leads to inhomogeneous spin dephasing that is characterized by the time T_2^*. It is typically shorter than T_2, being limited by quasi-static magnetic field fluctuations and ensemble inhomogeneities.

The coexistence of long coherence times and long spin polarization permanence at room temperature is a key feature that makes the NV center a unique solid-state quantum system.

2.2.5 Charge Conversion

2.3 Neutrally Charged NV

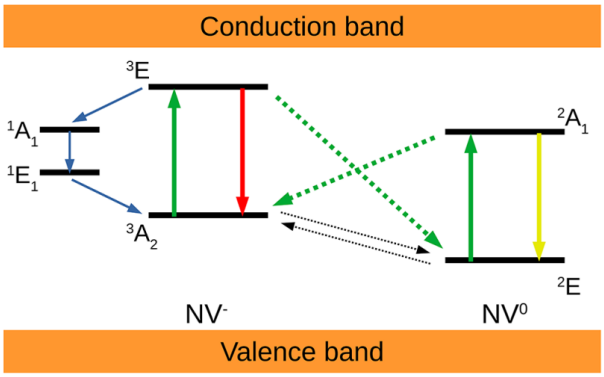

Source:(Gorrini *et al.*, 2021)

Figure 6 – Electronic dynamics scheme. Green arrows represent optical excitation (solid arrows) and charge conversion (dotted arrows). Red and yellow arrows indicate radiative decay from the excited levels of NV^- and NV^0, respectively. Blue arrows denote non-radiative intersystem crossing decay, and dotted black arrows indicate tunneling transitions in the dark between the NV^- and NV^0 ground states, responsible for restoring the NV^-/NV^0 population ratio to equilibrium.

The neutral charge state (NV^0) differs from NV^- primarily in its electronic structure. NV^0 has one fewer electron (5 electrons in total) and the ground-state, ^2E, is a spin doublet (spin-1/2) , with no DS_z^2 term and thus, with no zero-field splitting). Optically, NV^0 is characterized by a zero-phonon line at 2.156 eV (575 nm).

In ensemble measurements, additional effects such as charge-state dynamics may contribute to the effective decay times observed experimentally and while NV^0 is less commonly employed for magnetometry applications, it plays an important role in charge-state dynamics and photo-induced charge conversion processes, which is relevant for the characterization and understanding of NV ensembles.

A representation of the energy and charge state transitions is given in Figure 6

2.3.1 Ionization

Under optical excitation, the NV center can undergo charge-state conversion between NV^- and NV^0. Photoionization processes may promote an electron from the negatively charged defect into the conduction band, resulting in the transformation

$$NV^- \rightarrow NV^0 + e^-.$$

This process can occur via excitation to the ^3E state followed by ionization, and its probability depends on the excitation wavelength and laser intensity (Aslam *et al.*, 2013).There are indications that ionization occurs by two-photon absorption and an Auger process and does not require any other impurities close to the NV (Siyushev *et al.*, 2013):

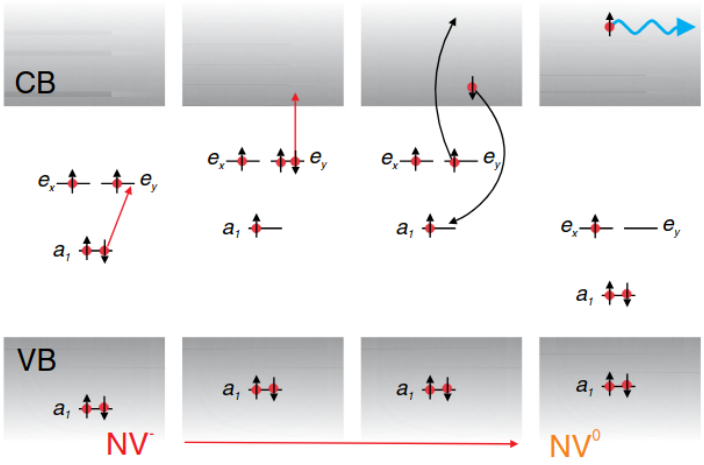

Source:(Siyushev *et al.*, 2013)

Figure 7 – Ionization of NV^-. Different occupation states slightly changes the energy levels as shown.

The first step is the excitation of NV^- ($a_1^2e^2 \rightarrow a_1e^3$) and while still excited, the NV might absorb another photon, promoting the electron to the **conduction band (CB)**. Recombination of this bound electron via an Auger process leads to the promotion of an

electron from an e orbital to the conduction band, leaving the NV in the NV^0 charge state. Ionization causes a sharp rise in the PL, and its influence is greater with more concentration of nitrogen and NV centers (Giri *et al.*, 2018). The system returns to equilibrium in the dark via charge-state tunneling transitions between the ground states of NV^- ($^3A_2$) and NV^0 (^2E)(black dotted arrow in Figure 6).

2.3.2 Back-conversion

The neutral charge state can capture an electron from the surrounding lattice or from nearby donor impurities, leading to charge recombination:

$$NV^0 + e^- \rightarrow NV^-$$

This recombination process can also be explained by a two-photon process (Figure 8).

Firstly, NV^0 is excited by absorption of a first photon promoting an electron to an e orbital. A second photon transfers an electron from the a_1 orbital in the valence band to the a_1 orbital in the bandgap before the radiative recombination of the excited state NV^0 , creating a hole in the a_1 orbital in the **valence band (VB)**. This hole migrates away from the NV center, leaving the NV in the negative charge state NV^-.

Back-conversion is responsible for a sharp rise in the NV^- population within the sample (Gorrini *et al.*, 2021). Similarly to the ionization case, equilibrium is reached via charge-state tunneling transitions between the ground states of NV^- ($^3A_2$) and NV^0 (^2E) (black dotted arrow in Figure 6).

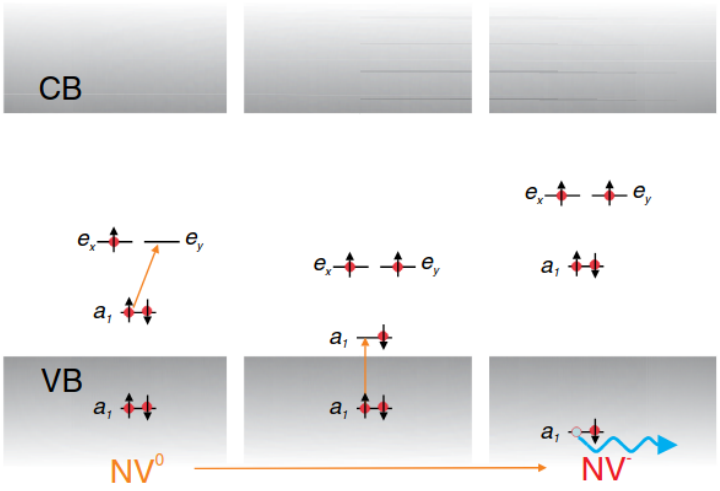

Source:(Siyushev *et al.*, 2013)

Figure 8 – Back-conversion $NV^0 \rightarrow NV^-$. Different occupation states slightly changes the energy levels as shown in the schematics

3 Starting model

3.1 Rate Equation Model

In general, the time evolution of an open quantum system such as the NV center can be described by the Lindblad master equation,

$$\frac{d\hat{\rho}}{dt} = -\frac{i}{\hbar}[\hat{H}_{\text{eff}}, \hat{\rho}] + \sum_{\alpha} \left(\hat{L}_{\alpha} \hat{\rho} \hat{L}_{\alpha}^{\dagger} - \frac{1}{2} \{ \hat{L}_{\alpha}^{\dagger} \hat{L}_{\alpha}, \hat{\rho} \} \right), \tag{3.1}$$

where ρ is the density matrix of the system, H_{eff} is the effective Hamiltonian, and the jump operators L_{α} describe dissipative processes such as spontaneous emission, spin-dependent intersystem crossing, and charge conversion. As an example, the Lindblad formalism has been employed in (Poggiali; Cappellaro; Fabbri, 2017) to measure the excited-state transverse hyperfine coupling.

The optical coherence time in the NV center is much shorter than the radiative lifetime, primarily due to strong vibronic coupling in the orbitally degenerate excited state ^3E, which induces rapid orbital mixing and dephasing (Fu *et al.*, 2009). This mechanism is not restricted to low temperatures. At room temperature, the orbital components of the excited state are averaged by thermal vibrations; thus, the excited state effectively exhibits the properties of an orbital singlet (Rogers *et al.*, 2009).

As a consequence, coherences between distinct electronic eigenstates, represented by the off-diagonal density matrix elements ρ_{ij} $(i \neq j)$, decay on timescales much shorter than those associated with population relaxation.

Under these conditions, the Lindblad equation reduces to a set of coupled differential equations involving only the level populations. Throughout this work, no coherence-generating terms are included in the Hamiltonian, nor are resonant microwave fields applied simultaneously with the green laser excitation (in such cases, this simplification would not be valid), justifying the rate-equation approach (Hincks; Granade; Cory, 2013).

We began this work by studying the model presented in (Song *et al.*, 2020), which focuses on optimizing the polarization efficiency of NV centers under optical excitation. That work adopts a rate-equation formalism written in matrix form, using transition rates reported in the literature.

The model simulates the population dynamics between the energy levels represented in Figure 5. The NV state is described by the population vector $\vec{P} = (P_1, P_2, P_3, P_4, P_5, P_6)$, where P_i is the population of sublevel $|i\rangle$ and $\sum_i P_i = 1$. We consider that the NV starting state is the thermal state given by $\vec{P}_0 = (\frac{1}{3}, \frac{2}{3}, 0, 0, 0, 0)$ meaning the ground state spin levels are evenly distributed between $m_s = 0, +1$ and -1.

The time evolution of $\vec{P}$ during an optical cycle is described by the rate equations, which in matrix form are given by:

$$\frac{d\vec{P}}{dt} = M\vec{P}. \tag{3.2}$$

Here, we take $M = M_0$ for the transition-rate matrix during laser pumping, and $M = M_1$ for the transition-rate matrix in the dark. The population transfer between levels $|i\rangle$ and $|j\rangle$ is described by k_{ij} (in ns^{-1}), with $k_{13} = k_{24} = a$ and $k_{31} = k_{42} = k$.

The main difference between both matrices are the laser-driven transitions. In this initial case, it is represented only by the transition from the ground state to the excited state ($k_{13} = k_{24} = a$), but other laser-driven transitions will appear later.

All transition rates related to the laser presence will be represented with the letter **a**. The dependence of these transition-rates with the laser properties are discussed in section 6.1.

The transition rates and the definitions of both matrices are given below.

Table 1 – Transition rates (ns^{-1})

a	k	k_{35}	k_{45}	k_{56}	k_{61}	k_{62}
0.099	0.0699	0.0049	0.0299	0.999	0.0032	0.0022

Note: Parameters from (Song *et al.*, 2020), divided by 2π. These parameters were gathered from different experiments in the literature.

$$M_0 = \begin{bmatrix} -a & 0 & k & 0 & 0 & k_{61} \\ 0 & -a & 0 & k & 0 & k_{62} \\ a & 0 & -(k+k_{35}) & 0 & 0 & 0 \\ 0 & a & 0 & -(k+k_{45}) & 0 & 0 \\ 0 & 0 & k_{35} & k_{45} & -k_{56} & 0 \\ 0 & 0 & 0 & 0 & k_{56} & -(k_{61}+k_{62}) \end{bmatrix} \tag{3.3}$$

and

$$M_1 = \begin{bmatrix} 0 & 0 & k & 0 & 0 & k_{61} \\ 0 & 0 & 0 & k & 0 & k_{62} \\ 0 & 0 & -(k+k_{35}) & 0 & 0 & 0 \\ 0 & 0 & 0 & -(k+k_{45}) & 0 & 0 \\ 0 & 0 & k_{35} & k_{45} & -k_{56} & 0 \\ 0 & 0 & 0 & 0 & k_{56} & -(k_{61}+k_{62}) \end{bmatrix} \tag{3.4}$$

3.1.1 Initial Improvements

The first modification introduced in this model was the splitting of the $m_s = \pm 1$ sublevels in both the ground and excited states, adding two additional energy levels and increasing the dimension from 6 to 8.

The goal was to reproduce the results of (Song *et al.*, 2020) within this extended Hilbert space. Breaking this degeneracy allows, in future works, the inclusion of spin–magnetic coupling interactions. Although the interaction of the NV center with external magnetic fields has not yet been considered in this work, all simulation results obtained so far are equivalent with and without the energy-level splitting, for all models described from this point onward.

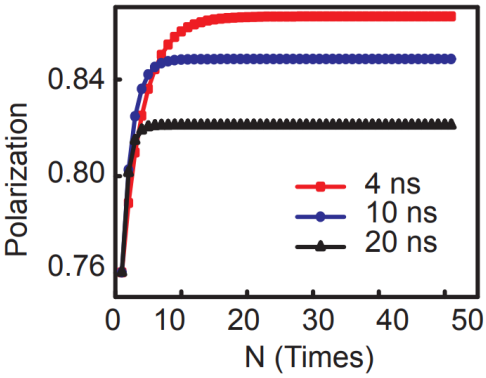

(a) Polarization vs Number of pulses for different pulse widths (Song *et al.*, 2020)

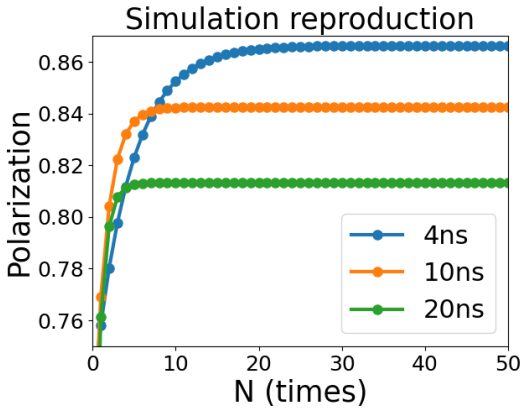

(b) Simulation reproduction.

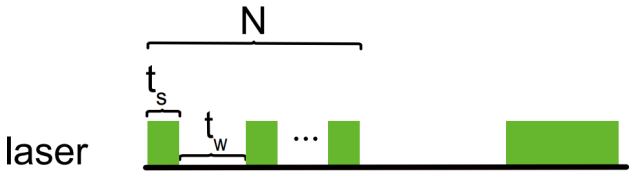

(c) Example of simulated experiment reproduced to verify the model.

Figure 9 – Comparison between simulation and measured data for 2 different experiments. The results from (a) and (b) are from the simulated experiment represented in (c) by tracking the P_1 population after each of the N pulses, where a train of N pulses of width t_s equally spaced by a wait time of t_w employed to polarize the NV. Final population P_1 for 4 ns pulse width is 86.6%.

3.2 Longitudinal Spin Relaxation

The experiments discussed in (Song *et al.*, 2020) are performed in a short-time regime and therefore do not take spin relaxation into account. Inspired by the model presented in (Tetienne; Hingant, *et al.*, 2013), we introduced longitudinal spin relaxation through the relation $1/T_1 = 3k_s$, where k_s is the transition rate between the ground-state sublevels $|0\rangle \leftrightarrow |+1\rangle$ and $|0\rangle \leftrightarrow |-1\rangle$.

This modification enables the simulation of the dark-time experiment performed in that work (Figure 10) and also clarifies the relation between the photoluminescence (PL)

signal and the level populations. Establishing this relation further allows the simulation of other time-resolved photoluminescence experiments, which will be discussed later.

The PL curve was simulated using the same transition rates from Table 1, together with $T_1 = 16$ μs (corresponding to $1/T_1 = 3k_s$). The authors have obtained this value of k_s by fitting their experimental data to the expression below.

$$\mathcal{I}(\tau) = \mathcal{I}(\infty)\left[1 - C_m e^{-t/T_m} + C_1 e^{-t/T_1}\right]. \tag{3.5}$$

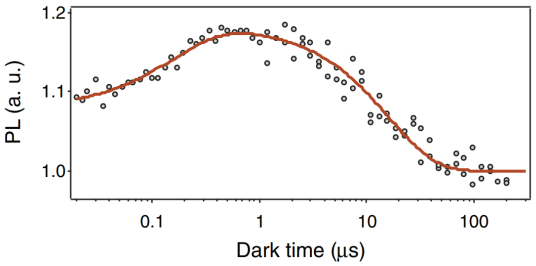

(a) PL versus dark time from (Tetienne; Hingant, *et al.*, 2013).

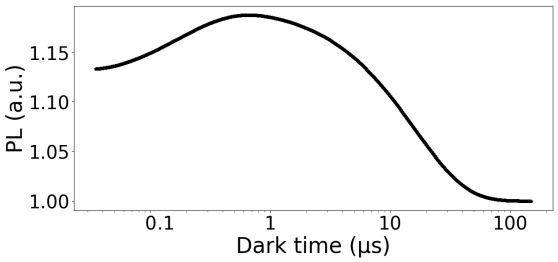

(b) Simulation result.

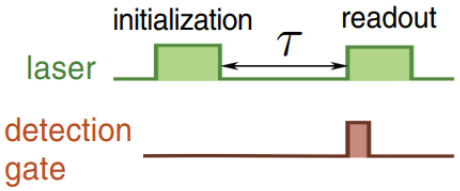

(c) Schematic representation of the experiment.

Figure 10 – Comparison between the experiment reported in (Tetienne; Hingant, *et al.*, 2013) and the simulation obtained with our model. The NV center is initialized by a 3 μs laser pulse, followed by a dark interval of duration τ. A probe pulse is then applied for PL detection, with a photon-detection gate of 300 ns. The photon counts are integrated within the detection window, producing a point on the y-axis of (a) corresponding to the chosen dark time between pulses.

The updated transition matrices are given by:

$$M_0 = \begin{bmatrix} -(a+2k_s) & k_s & k_s & k & 0 & 0 & 0 & k_{61} \\ k_s & -(a+k_s) & 0 & 0 & k & 0 & 0 & k_{62}/2 \\ k_s & 0 & -(a+k_s) & 0 & 0 & k_{42} & 0 & k_{62}/2 \\ a & 0 & 0 & -(k+k_{35}) & 0 & 0 & 0 & 0 \\ 0 & a & 0 & 0 & -(k+k_{45}) & 0 & 0 & 0 \\ 0 & 0 & a & 0 & 0 & -(k_{42}+k_{45}) & 0 & 0 \\ 0 & 0 & 0 & k_{35} & k_{45} & k_{45} & -k_{56} & 0 \\ 0 & 0 & 0 & 0 & 0 & 0 & k_{56} & -(k_{61}+k_{62}) \end{bmatrix} \tag{3.6}$$

and, for the laser-off configuration,

$$M_1 = \begin{bmatrix} -2k_s & k_s & k_s & 0 & 0 & 0 & 0 & k_{61} \\ k_s & -k_s & 0 & 0 & 0 & 0 & 0 & k_{62}/2 \\ k_s & 0 & -k_s & 0 & 0 & 0 & 0 & k_{62}/2 \\ 0 & 0 & 0 & -(k_{35}) & 0 & 0 & 0 & 0 \\ 0 & 0 & 0 & 0 & -(k_{45}) & 0 & 0 & 0 \\ 0 & 0 & 0 & 0 & 0 & -(k_{42}+k_{45}) & 0 & 0 \\ 0 & 0 & 0 & k_{35} & k_{45} & k_{45} & -k_{56} & 0 \\ 0 & 0 & 0 & 0 & 0 & 0 & k_{56} & -(k_{61}+k_{62}) \end{bmatrix} \tag{3.7}$$

Table 2 – Transition rates for the case where longitudinal spin relaxation is considered (ns^{-1})

a	k	k_{35}	k_{45}	k_{56}	k_{61}	k_{62}	k_s
0.099	0.0699	0.0049	0.0299	0.999	0.0032	0.0022	2.083×10^{-5}

Note: Parameters from (Song *et al.*, 2020), divided by 2π. These parameters were gathered from different experiments in the literature. The rate k_s was obtained by (Tetienne; Hingant, *et al.*, 2013) by fitting the curve shown in Figure 10(a).

The population vector is now defined as

$$\vec{P} = (P_1, P_{2m}, P_{2p}, P_3, P_{4m}, P_{4p}, P_5, P_6), \tag{3.8}$$

where the subscript m denotes the spin state $m_s = -1$ and p denotes $m_s = +1$. The initial thermal state is given by

$$\vec{P_0} = \left(\tfrac{1}{3}, \tfrac{1}{3}, \tfrac{1}{3}, 0, 0, 0, 0, 0\right). \tag{3.9}$$

3.2.1 Relation Between the PL Curve and the Model Matrices

In the supplemental material of (Tetienne; Hingant, *et al.*, 2013), Equation 3.5 is derived assuming a simplified four-level model and a short detection window (300 ns). Since our model successfully reproduces the PL curve via simulation, we need to establish the connection between the function describing this curve and the transition rates that define our eight-level model.

The analytical solution (Berberan-Santos; Martinho, 1990) for the population dynamics governed by Equation 3.2 is given by

$$\vec{P}(t) = e^{Mt}\vec{P}(0). \tag{3.10}$$

We define the emission rate $R(t)$, which is proportional to the population of the radiative excited states, as (Magaletti *et al.*, 2024):

$$R(t, \tau) = k\left[P_3(t, \tau) + P_{4m}(t, \tau) + P_{4p}(t, \tau)\right], \tag{3.11}$$

where k is the radiative transition rate and P_3, P_{4m} and P_{4p} are, respectively, the populations of the sublevels $m_s = 0, m_s = -1$ and $m_s = 1$ in the excited state.

To account for the photon counts detected experimentally, this rate must be integrated over the detection window. For the eight-level model, the PL signal can be written as

$$\mathrm{PL}(\tau) = \int_0^T R(t,\tau)\,dt = \sum_{i=1}^{8} A_i\, e^{\lambda_i \tau}, \tag{3.12}$$

where t denotes the detection window duration(in our case, the probe duration coincides with the detection window ranging, from 0 to the T), λ_i are the eigenvalues of M_1, and τ is the dark-time duration. The detailed derivation of this expression is presented in Appendix A.

Equation 3.11 is fundamental for the PL simulation in our model. The simulation is based on finding the evolution of the population, either with the laser on or of, and then integrating this emission rate for the detection window that corresponds to the probe pulse. This will return a PL x Dark time curve and Equation 3.12 allows us to fit the simulated curve (as shown in Figure 10) and extract the dominant eigenvalues from the exponential terms with the largest amplitudes.

The eigenvalues of M_1 (Equation 3.7) are:

Table 3 – Eigenvalues of M_1 defined in Equation 3.7.

Eigenvalue	Multiplicity
0	1
$-(k + k_{35})$	1
$-(k + k_{45})$	2
$-k_s$	1
$-3k_s$	1
$-k_{56}$	1
$-(k_{61} + k_{62})$	1

(Calculated with SymPy)

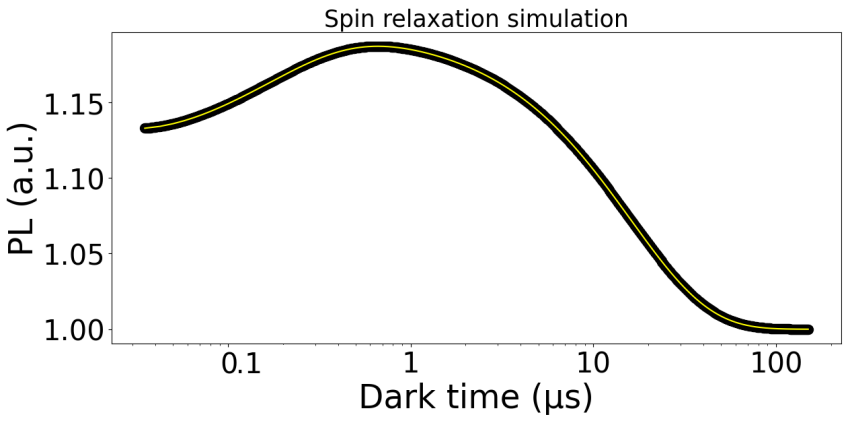

Figure 11 – Fit of the simulated PL curve using a multi-exponential model. The simulation is shown in black and the fit in yellow.

Table 4 – Fit parameters and corresponding characteristic times ($\tau_i = 1/|\lambda_i|$).

Mode	A_i	λ_i (numerical, ns^{-1})	τ_i (ns)	λ_i (analytical)
1	0.0442605	-0.075847	13.1844	$-(k + k_{35})$
2	-0.0812122	-0.00549723	181.91	$-(k_{61} + k_{62})$
3	0.197227	-6.25001×10^{-5}	1.6×10^4	$-3k_s$
		$C = 1.73981$		

The parameters that fit the curve shown in Figure 11 (yellow line) are listed in Table 4. We used Equation 3.12 to fit the simulated PL curve, but only three exponential terms were sufficient to describe the dominant features of the PL curve, indicating that the related processes are the most dominant when describing the dynamics.

The exponents obtained from the fitted exponential terms were equivalent to three (or four, considering the $\lambda_i = 0$ eigenvalue that is not a exponential in the final fit) of the eingenvalues of M_1 (Table 4) as expected, since we know from Equation 3.12 that the PL is a sum of exponential terms whose exponents are the eigenvalues of M_1. Since M_1 has 8 eigenvalues, it was expected 7 exponential terms, with one constant term related to $\lambda_i = 0$, but the fit only required three exponential terms, indicating the amplitudes for the terms related to the other eigenvalues are very small. The same result was obtained by explicitly calculating the PL expression using NumPy and SymPy with the previously defined matrices.

The amplitudes and characteristic times provide insight into the electronic dynamics of the NV center. Exponential terms with negative amplitudes correspond to a rise of the PL signal as a function of dark time, whereas positive amplitudes correspond to a PL decrease.

The characteristic time $\tau_i \approx 13$ ns is associated with the radiative decay of the excited state with $m_s = 0$. During optical initialization, the population becomes predominantly concentrated in P_3. The transition $P_3 \rightarrow P_1$ occurs with a characteristic time of approximately 13 ns. If the probe pulse arrives within this time scale, many electrons are still in the excited state, and the probe cannot excite as many additional electrons as it would immediately after initialization. As the dark time increases beyond this scale, the excited-state population decays, modifying the detected PL accordingly.

The characteristic time $\tau_i \approx 181$ ns is related to the non-radiative decay pathway through the metastable state. Electrons that decay through intersystem crossing are transferred to the metastable level and remain there temporarily. The decay from P_6 to the ground-state sublevels occurs on a time scale of approximately 180 ns and is spin-selective, preferentially repopulating P_1. As a consequence, for dark times longer than

this characteristic time, the population in $|0\rangle$ increases, enhancing the PL signal when the probe pulse is applied.

Finally, the characteristic time of approximately 16 μs corresponds to longitudinal spin relaxation. This value was extracted from (Tetienne; Hingant, *et al.*, 2013) and incorporated into our model through the rate k_s. The fit of the simulated PL curve recovers this same time scale explicitly as one of the dominant exponential terms, whose exponent is precisely the eigenvalue $-3k_s$ of M_1, demonstrating that the added relaxation rate manifests itself in the PL dynamics. This result indicates that a PL dark-time experiment can be used to extract T_1 directly from our NV sample. At long dark times, spin relaxation progressively mixes the ground-state populations, reducing the degree of spin polarization. This depolarization decreases the PL signal and ultimately drives the system toward the thermal state (Equation 3.9).

In contrast to Equation 3.5, an additional exponential associated with τ_1 (Table 4) appears in our fit. The model in (Tetienne; Hingant, *et al.*, 2013) considers only the metastable level and the three ground states, neglecting the explicit contribution of the excited-state dynamics. Experimentally, resolving this fast exponential contribution is challenging: the probe pulse duration must be much shorter than 13 ns, and precise control of short dark times is required. These experimental constraints may prevent the clear observation of this additional exponential term in measured PL profiles, which will also be the case in our experiments, as discussed later.

3.3 PL Lifetime Experiment

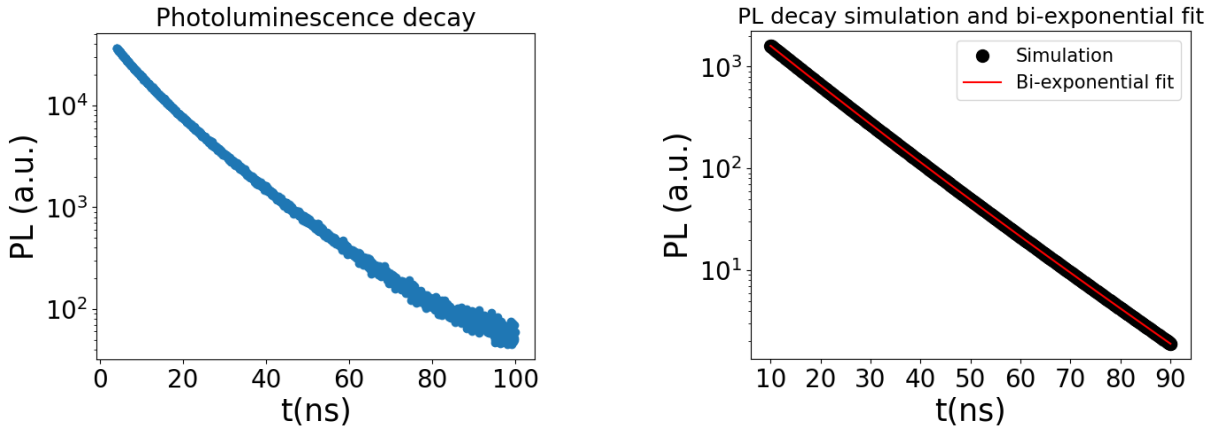

(a) Example of a emission decay curve measured in our laboratory.

(b) Simulation (black) and bi-exponential fit (red).

Figure 12 – Comparison between an experimental result from our laboratory and the corresponding simulation. Fit parameters are listed in Table 5.

Optical excitation followed by time-resolved photoluminescence detection provides a direct method to determine the excited-state lifetime. This lifetime is related to the

emission rate (Equation 3.11) and, consequently, to the characteristic decay times $1/(k+k_{35})$ for P_3 and $1/(k+k_{42})$ for P_{4m} and P_{4p}.

Table 5 – Fit parameters and corresponding characteristic times ($\tau_i = 1/|\lambda_i|$) for the PL decay experiment Figure 12(b).

Corresponding spin state	A_i	τ_i	λ_i
$m_s = 0$	1337.63	13.34	$-(k+k_{35})$
$m_s = \pm 1$	2641.68	10.00	$-(k+k_{45})$

Similarly to the procedure described in the previous section, a bi-exponential function can be fitted to the simulated emission decay curve, allowing the recovery of the eigenvalues of M_1 associated with the excited-state decay. The experiment consists of applying a short optical pulse followed by time-resolved detection of the emitted PL. In this way, the decay of the excited-state population after the excitation pulse can be directly observed.

The simulation is performed by starting from the thermal state and applying a short excitation pulse (10 ns for the result shown in Figure 12), followed by plotting the emission rate as a function of time after the pulse.

This experiment does not involve optical initialization; therefore, there is no "dark time", which in the previous section was defined as the time interval between the initialization pulse and the probe pulse. Consequently, the emission rate is written as

$$R(t) = k\left[P_3(t) + P_{4m}(t) + P_{4p}(t)\right],$$

where t denotes the time starting after the excitation pulse.The results are shown in Figure 12 and summarized in Table 5. From the amplitudes A_i obtained in the bi-exponential fit, it is possible to infer that the NV center was initially in the thermal state. In particular, the amplitude associated with the $m_s = 0$ component is approximately half of that associated with the $m_s = \pm 1$ component. This ratio between both amplitudes is consistent with the population distribution expected for the thermal state described in Equation 3.9. This result can be obtained by calculating the dynamics directly from Equation 3.2 for the thermal state, and later we will observe the approximately the same ratio when we discuss the fit for Figure 12(a)(Table 11).

Together with the dark-time experiment discussed previously, this measurement allows the extraction of most eigenvalues of M_1, which governs the electronic dynamics of the NV center in the dark.

Combined, these two experiments yield the of M_1, and from these eigenvalues, the transition rates can be estimated, establishing a clear recipe for the characterization of a given sample.

The transition rate k_{56} requires a different approach and will be neglected in the final model. As observed in Table 1, this rate corresponds to a much faster decay compared to

the other characteristic times in the electronic dynamics. Therefore, it will be treated as effectively instantaneous, reducing the singlet manifold to a single effective level.

3.4 Ionization process

The next step on the develop of our model is to include the ionization process on our considerations. This addition was inspired by the PL profile of one bulk NV sample available in our laboratory. The main reference suggesting that a sharp rise in the PL could be due to the ioniztion of the NV($NV^- \rightarrow NV^0$) is (Giri *et al.*, 2018). The natural approach is to add 1 extra level corresponding to the NV^0, P_7, to our so-far 8-level model.

The ionization process is assumed to be spin-independent (the same is assumed for the natural recharge process), meaning that the reported characteristic time is related to the transition rates by $1/T_r = (k_{71} + k_{72m} + k_{72p}) = 3k_{ion}$ with $T_r \approx 100\mu s$ being the recharge time for $NV^0 \rightarrow NV^-$.

This relation between the recharge time and the recharge rates differs from that of the reference paper, in which the authors employ a simplified four-level model that includes a metastable level representing collectively the excited NV^- states, the singlet state, and the NV^0 charge state.

In contrast, we adopt a more explicit modeling strategy, introducing specific transition rates for $P_{ES} \rightarrow P_7$ and $P_7 \rightarrow P_{GS}$, where P_{ES} and P_{GS} denote the total excited-state and ground-state populations, respectively.

These transitions are represented in Figure 6. $P_{ES} \rightarrow P_7$ is indicated by the dotted green arrow connecting ${}^3E \rightarrow {}^2E$ and $P_7 \rightarrow P_{GS}$ is denoted by the dotted black arrow connecting ${}^2E \rightarrow {}^3A_2$. It is worth mentioning that neither the NV^0 internal dynamics nor the back-conversion ($NV^0 \rightarrow NV^-$ via photon absorption) are considered at this point.

The new matrices are:

$$M_0 = \begin{bmatrix} -(a+2k_s) & k_s & k_s & k & 0 & 0 & 0 & k_{61} & k_{ion} \\ k_s & -(a+k_s) & 0 & 0 & k & 0 & 0 & k_{62}/2 & k_{ion} \\ k_s & 0 & -(a+k_s) & 0 & 0 & k_{42} & 0 & k_{62}/2 & k_{ion} \\ a & 0 & 0 & -(k+k_{35}+a_{ion}) & 0 & 0 & 0 & 0 & 0 \\ 0 & a & 0 & 0 & -(k+k_{45}+a_{ion}) & 0 & 0 & 0 & 0 \\ 0 & 0 & a & 0 & 0 & -(k+k_{45}+a_{ion}) & 0 & 0 & 0 \\ 0 & 0 & 0 & k_{35} & k_{45} & k_{45} & -k_{56} & 0 & 0 \\ 0 & 0 & 0 & 0 & 0 & 0 & k_{56} & -(k_{61}+k_{62}) & 0 \\ 0 & 0 & 0 & a_{ion} & a_{ion} & a_{ion} & 0 & 0 & -3k_{ion} \end{bmatrix} \tag{3.13}$$

and, for the laser-off configuration,

$$M_1 = \begin{bmatrix} -2k_s & k_s & k_s & 0 & 0 & 0 & 0 & k_{61} & k_{ion} \\ k_s & -k_s & 0 & 0 & 0 & 0 & 0 & k_{62}/2 & k_{ion} \\ k_s & 0 & -k_s & 0 & 0 & 0 & 0 & k_{62}/2 & k_{ion} \\ 0 & 0 & 0 & -(k_{35}) & 0 & 0 & 0 & 0 & 0 \\ 0 & 0 & 0 & 0 & -(k_{45}) & 0 & 0 & 0 & 0 \\ 0 & 0 & 0 & 0 & 0 & -(k_{42}+k_{45}) & 0 & 0 & 0 \\ 0 & 0 & 0 & k_{35} & k_{45} & k_{45} & -k_{56} & 0 & 0 \\ 0 & 0 & 0 & 0 & 0 & 0 & k_{56} & -(k_{61}+k_{62}) & 0 \\ 0 & 0 & 0 & 0 & 0 & 0 & 0 & 0 & -3k_{ion} \end{bmatrix} \tag{3.14}$$

and the population vector is now defined as

$$\vec{P} = (P_1, P_{2m}, P_{2p}, P_3, P_{4m}, P_{4p}, P_5, P_6, P_7), \text{ and } \vec{P}_0 = \left(\tfrac{1}{3}, \tfrac{1}{3}, \tfrac{1}{3}, 0, 0, 0, 0, 0, 0\right) \tag{3.15}$$

with a_{ion} being the ionization rate at which electrons in the excited state are promoted to the conduction band, converting the NV center into the NV^0 charge state and k_{ion} the recharge rate that follows $1/T_r = 3k_{ion}$.

We performed a simulation of a dark-time experiment similar to the one described in section 3.2. The pulse sequence is shown in Figure 13(a).

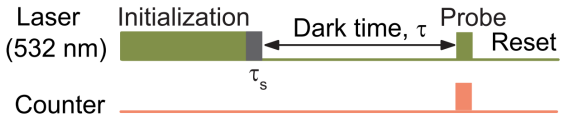

(a) Pulse sequence for the dark-time experiment. After a 500 μs initialization pulse, an additional dark interval $\tau_s = 1$ μs is introduced to enhance polarization into the $m_s = 0$ state. The dark time τ does not include τ_s. A 1 μs probe pulse is then applied, with a detection window (red) of 1 μs.

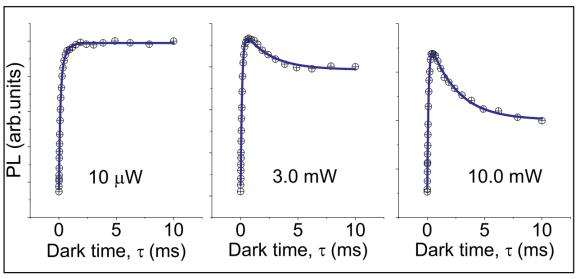

(b) PL as a function of dark time for different laser powers, reproduced from (Giri *et al.*, 2018).

Figure 13 – Dark-time experiment performed on a high-density NV ensemble, adapted from (Giri *et al.*, 2018).

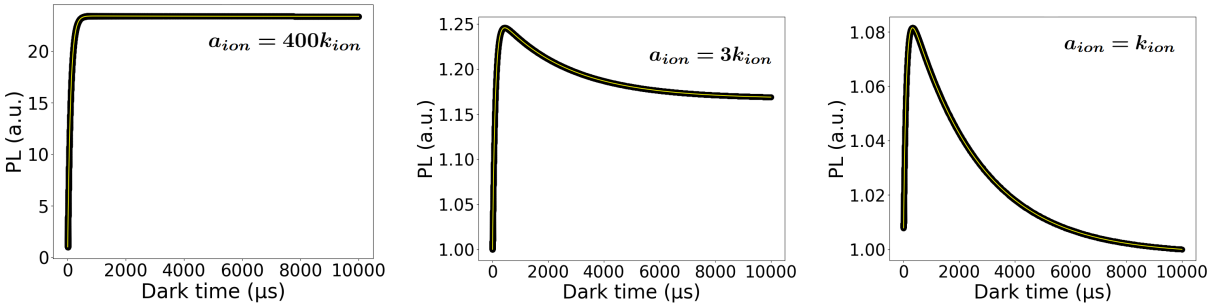

(a) PL curve for ionization rate $a_{ion} = 400k_{ion}$.

(b) PL curve for ionization rate $a_{ion} = 3k_{ion}$.

(c) PL curve for ionization rate $a_{ion} = k_{ion}$.

Figure 14 – Simulation of the dark-time experiment showing how the PL curve depends on laser power. The parameter varied is a_{ion}. Black curves correspond to the simulated PL, and yellow curves represent the multi-exponential fit.

The simulation qualitatively reproduces the behavior observed in Figure 13(b). Since a bulk NV ensemble is considered (in contrast with the previous models), the value of T_1 was replaced to better represent ensemble dynamics. The value adopted was $T_1 = 2.5$ ms, based on the relaxation profile observed in the experimental PL curves reported in (Giri *et al.*, 2018).

In this case, the matrix M_1 has one additional dimension compared to the previous model, leading to one extra eigenvalue. The eigenvalues remain the same as those listed in Table 3, with the addition of $-3k_{ion}$.

Table 6 – Eigenvalues of the M_1 matrix defined in Equation 3.14.

Eigenvalue	Multiplicity
0	1
$-(k + k_{35})$	1
$-(k + k_{45})$	2
$-k_s$	1
$-3k_s$	1
$-k_{56}$	1
$-(k_{61} + k_{62})$	1
$-3k_{ion}$	1

(Calculated with SymPy)

Table 7 – Fit parameters and corresponding characteristic times ($\tau_i = 1/|\lambda_i|$) for the PL curve in Figure 14(c).

Mode	A_i	λ_i (numerical, ns^{-1})	τ_i ns	λ_i (analytical)
1	0.0990072	$-4\text{x}10^{-7}$	$2.5\text{x}10^{-6}$	$-3k_s$
2	−0.0898554	$-1\text{x}10^{-5}$	100000	$-3k_{ion}$
3	−0.0750424	−0.00549737	181.9	$-(k_{61} + k_{62})$
4	−0.008048	−0.0749642	13.33	$-(k + k_{35})$
$C = 1.73981$				

The PL curve can still be fitted by a multi-exponential model, and the most dominant components are summarized in Table 7. Once again, it was possible to recover the eigenvalues of M_1 from this fit, and consequently some of the transition rates associated with these eigenvalues.

In the reference paper, the authors obtained different PL curves by varying the laser power. The rates a and a_{ion} correspond to excitation and ionization processes, respectively, and are therefore expected to depend on the laser power. The discussion about these parameters are on section 6.1.

It is worth mentioning that the behavior observed for the PL curve in Figure 13 (b) occurs when the laser power is increased. In the simulation result, we obtain the opposite. That is because a fixed k_{ion} was used in the simulation for simplicity reasons. In (Aslam *et al.*, 2013) it is discussed that the rates represented in this work by a_{ion} and k_{ion} might depend quadratically on the laser power. The recombination rate k_{ion} in itself was not of interest for our simulation, our main goal was to re-obtain it from the PL curve fit.

Table 8 – Additional transition rates for the ionization simulation

Rate	Values (ns^{-1})
a	0.07976
k_s	1.4×10^{-7}
k_{ion}	3.4×10^{-6}

Values for a_{ion} can be found in Figure 14. Other rates are the same as in Table 1

4 Experiments and Data

The discussion in the previous chapter shows that, by fitting multi-exponential functions to both a dark-time experiment (section 3.2) and a PL lifetime decay experiment (section 3.3), it is possible to obtain most of the eigenvalues of the matrix M_1, which describes the internal transitions of the NV center independently of laser excitation.

The exponents of the multi-exponential profile that governs the NV photoluminescence curve are related to characteristic times associated with different mechanisms within the NV electronic structure. These exponents correspond to the eigenvalues of M_1, and the relation between a characteristic time and its respective eigenvalue is given by $\tau_i = 1/\lambda_i$.

From these eigenvalues, it is possible to infer the transition rates associated with each process and construct the matrices describing the electronic dynamics. After reproducing the results discussed in the previous chapter, the next step is to perform the corresponding experiments and characterize a sample from our laboratory, validating the extracted rates through simulations of the same experimental procedures.

This procedure can be applied to any sample. First, the relevant physical processes must be identified and the experiments required to determine the corresponding transition rates are then performed. Once these rates are obtained, they can be used to build a model describing the NV dynamics, which can subsequently be used to simulate the experiments and, ideally, reproduce the experimental data.

4.1 Setup

The experiments were performed using a PicoQuant MicroTime 200 confocal microscope platform at QuantumTec, the quantum technology laboratory of the Centro Brasileiro de Pesquisas Físicas (CBPF). The investigated sample is a DNV-B14 diamond from Element Six, a single-crystal diamond grown by chemical vapor deposition (CVD) containing a controlled density of NV centers. This material is designed for experiments employing NV ensembles and typically presents an NV concentration of approximately 4.5 ppm. The characteristic spin coherence times reported for this material are of the order of $T_2^* \sim 0.5\,\mu s$ and $T_2 \sim 10\,\mu s$, making it suitable for ensemble-based sensing experiments. (Element Six, 2021)

Optical excitation is provided by diode lasers with wavelength $\lambda = 509\,\text{nm}$ controlled by a Sepia PDL 828 multichannel picosecond diode laser driver. This unit allows precise control of the laser triggering and timing parameters used in the experiments. It also allows the selection of CW or pulsed modes. The emitted photoluminescence is collected through the confocal microscope and directed to single-photon detectors.

Photon detection is performed using single-photon avalanche photodiodes (SPADs) from the PDM series (τ-SPAD) as well as photomultiplier tubes (PMTs), depending on the measurement configuration. Time-resolved measurements are carried out using the time-correlated single photon counting (TCSPC) technique. The TCSPC acquisition is implemented with a HydraHarp 400 multichannel picosecond event timer electronic module, which records photon arrival times with picosecond resolution.

The experimental sequence, including laser control, synchronization and data acquisition, is automated using custom Python scripts that interface with the hardware components of the setup.

4.2 Experimental Procedures and Data

The easiest and more direct experiment is the PL lifetime measurement. A short green (509 nm) laser pulse of 25 ns duration is applied to the NV in thermal state and we measure how the photon counts behave as a function of time which can be seen in Figure 15 on the next section. This simple experiment allow us to estimate k, k_{35} and k_{45} as discussed in section 3.3. The bi-exponential fit is in Figure 24 and the parameters obtained from the fit are in Table 11.

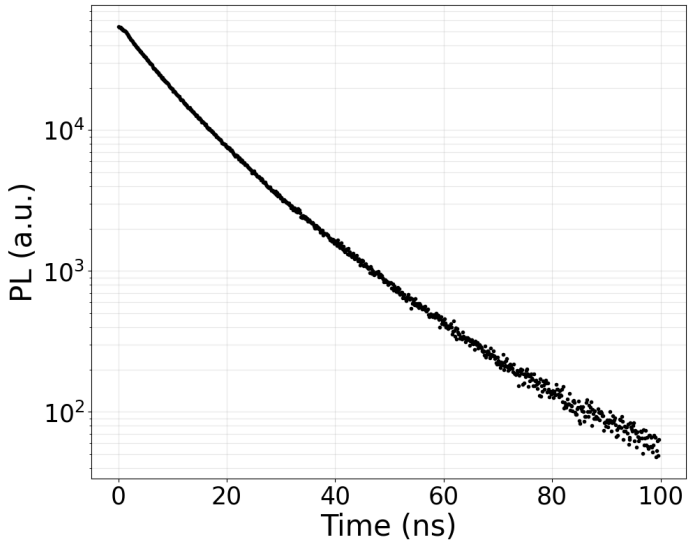

Figure 15 – Bi-exponential decay of the photon count over time.

The remaining eigenvalues can be extracted from the dark-time experiment discussed in section 3.2 and section 3.4. Initially, it was performed an experiment similar to the one described in Figure 10 **(c)**, expecting a rise in the PL signal due to the preferential relaxation from the metastable state into the $m_s = 0$ ground state. Additionally, if the laser effectively ionized the sample, a sharper increase associated with electron recombination could also be observed.

However, the measured PL curve presents a different and unexpected behavior. The increase in PL abruptly stops around 250 ns, followed by a smooth decrease until approximately 5 μs (Figure 17). After this point, the PL increases again, most likely due to the recombination of ionized NV centers, and is then followed by an exponential decay attributed to spin relaxation.

After some consideration, the possibility that the laser could be creating NV^- centers was taken into account. This led to a small modification in the final experimental protocol (Figure 16). A 500 μs laser pulse is applied after an initialization pulse (also 500 μs), with a dark interval of duration τ between them. The photon counts are now integrated within two detection windows of 1 μs each.

The total photon count within the first detection window will be referred to as $PL_{initial}$. From the initialization pulse until the end of this initial window, the experiment is identical to the one described in Figure 10. The PL integrated over the final window will be referred to as PL_{final} and should provide information about how the steady state changes with the dark time.

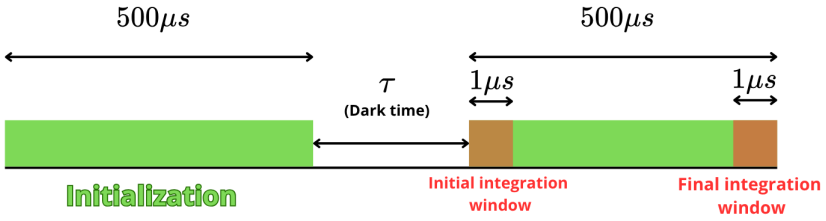

Figure 16 – Experiment performed to collect the PL in an initial detection window ($PL_{initial}$) and the PL integrated over the final detection window (PL_{final}). These detection windows (red) correspond to the first and last 1μs of the 509 nm laser pulse (Green), respectively.

If NV saturation is achieved, PL_{final} should remain constant, since the saturation PL is not expected to depend on the dark-time interval. However it was observed that the saturation PL decreases after around 1 μs of dark time (Figure 18).

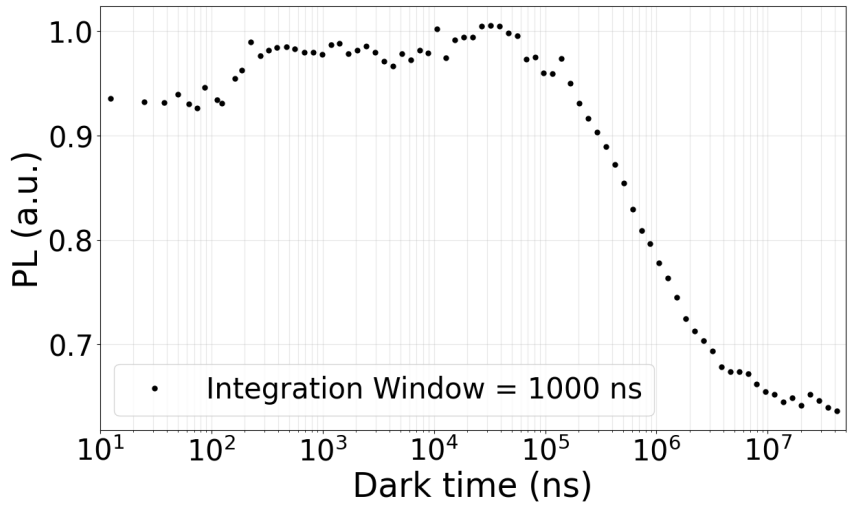

Figure 17 – $PL_{initial}$. Result from our PL versus Dark-Time experiment. This curve is obtained by the integration over the initial detection window plotted versus the dark time between the two pulses.

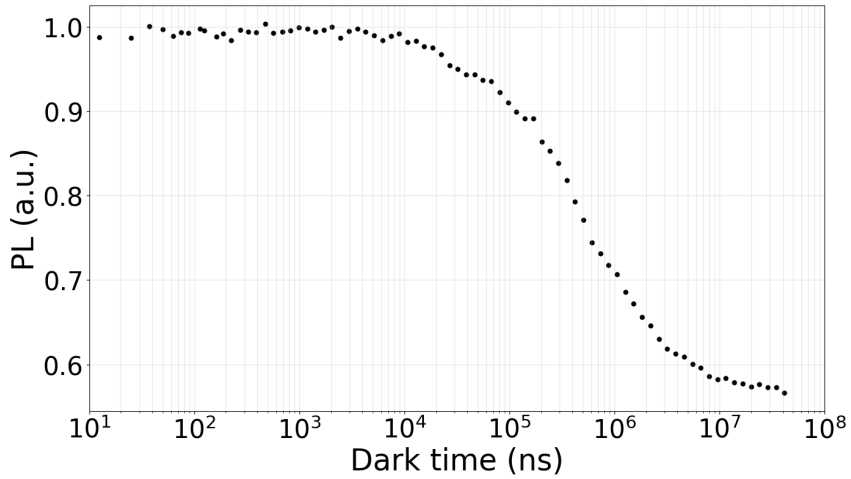

Figure 18 – PL_{final}. PL integrated over the final detection window ($1\mu s$) versus the dark time (τ) between the two pulses.

The curve in Figure 18 shows that PL_{final} which should be the photoluminescence of saturation (PL_{sat}), reaches a maximum. If the NV sample experiences a long period in the dark (over 1 μs) the PL_{sat} drops, indicating that the number of negatively charged NV decreases in the dark (and increases with laser excitation), reaching almost half of the PL for short duration dark times.

The PL_{sat} is maximum if the sample reaches a maximum of negatively charged NV NV^-_{sat}. The fact that the number of NV^- almost doubles is reported for shallow NV crystals in (Gorrini *et al.*, 2021).

The experiment was repeated for different laser power settings, and the same PL profile previously shown in Figure 17 was observed. The laser power is obtained by a power meter inside the equipment, and it can be read, in arbitrary units, in the software before

the experiment begins. The photon count is measured by the detector, and was taken immediately before the experiment begins, in order to compare between different laser power settings.

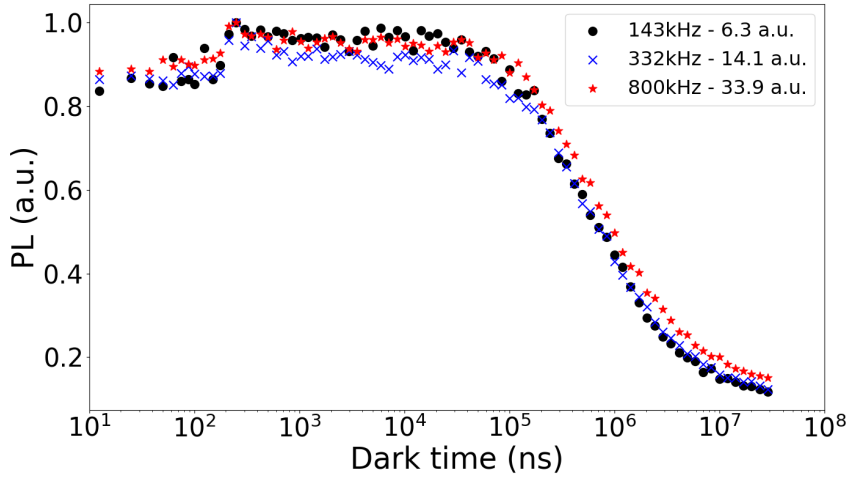

Figure 19 – $PL_{initial}$ for different laser power settings. In the inset legend, the first value corresponds to the photon detection rate, while the second indicates the laser power in arbitrary units. The PL is normalized such that its maximum value is equal to 1.

For all three cases considered, the normalized PL curves nearly overlap, indicating that the temporal profile of the photoluminescence, when expressed relative to its maximum value, is largely independent of the laser power within the explored range.

In particular, the maximum PL occurs at a dark time of 250 ns. This local maximum, also visible in Figure 17, suggests the existence of an optimal dark time for protocols that aim to maximize the photoluminescence signal from the sample.

The figure below is the non-normalized PL. The emitted photoluminescence is greatly increased with laser power, as expected.

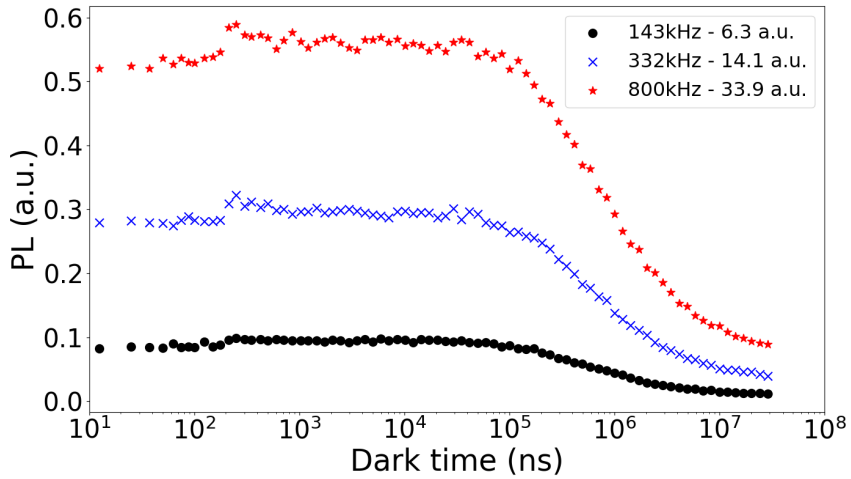

Figure 20 – Non-normalized $PL_{initial}$ for different laser power settings. In the inset legend, the first value corresponds to the photon detection rate, while the second indicates the laser power in arbitrary units.

These experimental results show indications of charge conversion. The sudden decrease in the PL is an indicative of back-conversion by light absorption during laser pumping, and the rise in the PL around $3\mu s$ is also an indicative that the NV was ionized while exposed to light. This is discussed in the next chapter.

5 Final Model

5.1 Initial Considerations

The experimental data indicate that the DNV-B14 sample exhibits pronounced charge conversion dynamics even under low-power green laser excitation. The measurements reveal clear signatures of both ionization ($NV^- \rightarrow NV^0$) and back-conversion ($NV^0 \rightarrow NV^-$), which makes it necessary to explicitly include both processes in the modeling.

In the following model, ionization and back-conversion are treated as independent processes. This choice is motivated by several considerations. First, enforcing a strictly coupled description between NV^- and NV^0 populations would require a detailed inclusion of the internal dynamics of the NV^0 center, as well as additional sample-dependent parameters such as NV^0 density. This would significantly increase the complexity of the model and the experimental procedures to support such level of detail.

Second, ionization and back-conversion are governed by distinct physical mechanisms and are often treated separately in the literature. Previous studies report regimes in which one process dominates over the other depending on the experimental conditions and sample properties. For instance, ionization is the dominant mechanism in (Giri *et al.*, 2018), where it is associated with high nitrogen and NV center densities, which favor charge transfer processes. On the other hand, back-conversion plays the leading role in (Gorrini *et al.*, 2021), where the sample geometry are taken in consideration.

Additionally, as will be shown later, the experimental data can only be fitted by an expression that explicitly separate these contributions. In the Stretched Exponential Model (section 5.2), the back-conversion process is described by a stretched exponential term that modulates the solution of the rate equations, related to the back-conversion and the rate-equation dynamics requires three exponential contributions to reproduce the observed dynamics; one associated with decay through the metastable state, one with longitudinal spin relaxation, and the last additional contribution associated with ionization.

As discussed in section 3.4, the effect of ionization on the PL can be accurately reproduced by incorporating it as an additional population channel within a rate-equation-only model.

The separation between ionization and back-conversion allows for a more direct physical interpretation of the fitted parameters enabling their consistent use in simulations to reproduce the experimental results. As such, the fitted parameters can be interpreted as an effective characterization of the sample under the specific experimental conditions, while also facilitating direct comparison with values reported in the literature.

It is important to emphasize that our model takes in consideration that the variations in the NV^- population are assumed not to introduce additional interactions, such as

NV–NV coupling, nor to modify the intrinsic transition rates during the charge dynamics. This suggests that the transition rates obtained from the model should be interpreted as effective parameters that describe the net dynamical behavior of the system, rather than as fundamental microscopic constants.

Finally, the metastable manifold was reduced to a single effective level. Since the detailed dynamics within the metastable states are not the primary focus of this work, the transition rate between levels $|5\rangle$ and $|6\rangle$ is assumed to be sufficiently fast to justify its elimination. This reduction to a one-dimensional effective subspace significantly simplifies the calculation of the eigenvalues of the dark-dynamics matrix M_1.

5.2 Stretched Exponential Model

5.2.1 The Stretching Exponential Factor

Following the results from (Gorrini *et al.*, 2021), summarized in Figure 3 of their paper (Figure 21 in this document), the number of NV^0 centers decreases as a function of two main parameters of the pumping laser: the laser power and the pulse duration. Similarly, after laser excitation, the population of NV^0 increases in the dark, with a characteristic time that also depends on these parameters.

Their experimental data were fitted using a stretched exponential function of the form:

$$I(t) = I_{eq}\left(1 \pm Ce^{-(\frac{t}{T})^m}\right) \tag{5.1}$$

This expression describes the temporal evolution of the photoluminescence (PL). The $+$ sign corresponds to the decrease of the NV^0 emission under laser excitation, while the $-$ sign represents the dark regime, where the NV^0 population increases. The stretching factor "m" is a number between 0 and 1. The rate of back-conversion is called $a_{bc} = 1/T_{NV^0 \to NV^-}$, related to the decrease of NV^0 under laser excitation. The rate of relaxation of this process in the dark, which is of greater interest in this work, is $k_{bc} = 1/T_{NV^- \to NV^0}$.

The experiments were performed by them under a strong magnetic field (750 G). In this regime, spin states are mixed, which suppresses the optical spin polarization into the $m_s = 0$ state for the NV^- charge state. As a result, the observed PL variations can be predominantly attributed to charge dynamics.

In Figure 21 (a) is shown how the NV^0 fluorescence behaves for different illumination times. The longer the pulse, less NV^0 is detected, implying that the laser is directly responsible for the $NV^0 \to NV^-$conversion. In Figure 21 (b) a similar experiment to Figure 10 (c) is performed by (Gorrini *et al.*, 2021). It is possible to observe from their results that, after the sample experiences a dark time, the NV^0 fluorescence rises. Both results indicate that NV^0 is converted to NV^- due to the laser presence, and then NV^- is converted back to the neutral state after a dark time. This is confirmed by Figure 21 (c),

where the population of both charge states is monitored during the dark time experiment, and the result shows that while NV^0 population increases, the population of NV^- increases, and the sum of populations is constant (yellow triangles).

In the same work, it is shown that the population dynamics of the charge states can also be described by a stretched exponential. The back-conversion process ($NV^0 \rightarrow NV^-$) and the relaxation in the dark ($NV^- \rightarrow NV^0$) arise from different physical mechanisms; therefore, their characteristic times and rates are, in general, different ($a_{bc} \neq k_{bc}$).

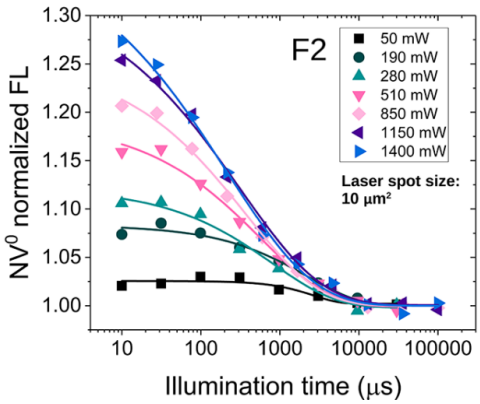

(a) Figure 3 (b) from (Gorrini *et al.*, 2021).

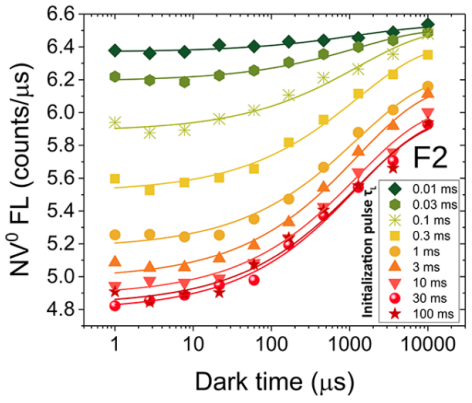

(b) Figure 3 (d) from (Gorrini *et al.*, 2021).

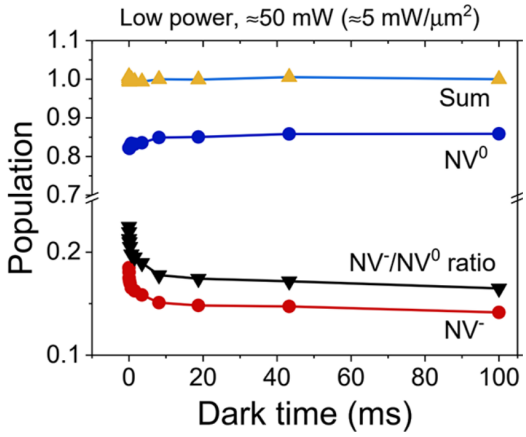

(c) Figure 5 (b) from (Gorrini *et al.*, 2021).

Figure 21 – Variation of NV^0 and NV^- populations and the corresponding PL dynamics due to charge conversion, fitted using a stretched exponential model.

The experiment performed in this work (chapter 4) was conducted in a low-power regime. The diode current was set to 50% (with NV excitation ceasing around 46%), corresponding to approximately 20 a.u. of power. Although this value is typically converted into optical power in μW, a calibration table for the 509 nm laser is not currently available.

By comparison with the calibration for a 532 nm laser, the optical power is estimated to be on the order of 100 μW, which is consistent with the green-circle data in Figure 21(a).

The pulse duration used was 500 μs, corresponding to a regime between the yellow (square dots) and orange (circle dots) curves in Figure 21(b).

These experimental conditions allow for an approximation that significantly simplifies the simulation: the characteristic times for back-conversion and relaxation are taken to be equal. Since the laser-on dynamics are beyond the scope of this work, this assumption reduces the number of free parameters in the stretched exponential model, eliminating the need to independently fit both the characteristic time and the stretching exponent for each process.

The following model takes in consideration that the PL expression in time is fitted by an expression similar to the Rate-Equation (sum of exponentials) modulated by the expression Equation 5.1

$$I(\tau) = I_{eq}\left(1 + Ce^{-(k_{bc}\tau)^n}\right)\left(\sum_{i=1} A_i\, e^{\lambda_i \tau}\right) \tag{5.2}$$

with $0 < n < 1$. The derivarition of this expression is found in Appendix B.

5.2.2 The Model

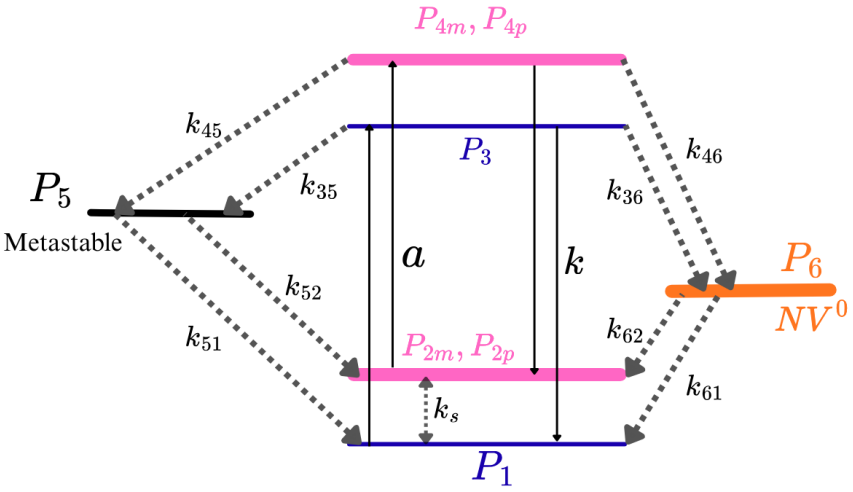

Figure 22 – Eight-level model for the spin and charge dynamics of the NV. Blue and pink levels represent the $m_s = 0$ spin states and $m_s = \pm 1$, respectively. The black level (P_5) comprises the metastable manifold as a single effective level, and the orange level P_6 denotes the ionization channel of NV^-, where the ionization rates are k_{36} and k_{46}. The rates k_{61} and k_{62} correspond to the recombination process.

The energy-level structure and the transitions between them are represented in Figure 22. This model is similar to the one introduced in section 3.4, incorporating the ionization process through additional transition rates. The transition rates are assumed to be spin-

independent and are therefore defined as $k_{36} = k_{46} = a_{ion}$, corresponding to the ionization rate, and $k_{61} = k_{62} = k_{ion}$, corresponding to the recombination rate.

The population P_6 represents the fraction of NV^- centers that are ionized via a two-photon absorption process (Figure 7) and subsequently recombine, returning to the NV^- charge state.

The populations P_{2m} and P_{2p} correspond to the two degenerate ground-state levels with spin projections $m_s = -1$ and $m_s = +1$, respectively. All transitions associated with these populations are identical for both spin projections , i.e. k_{45} is valid for the two transitions: $P_{4m} \to P_5$ and $P_{4p} \to P_5$. The same symmetry applies to the excited-state populations P_{4m} and P_{4p}. This explicit separation may become relevant in future extensions of the model, particularly if interactions with an external magnetic field are introduced.

The contribution of the back-conversion process to the PL curve is captured by the stretched-exponential factor introduced in Equation 5.2. While the internal dynamics described in Figure 22 remain governed by the matrices M_0 and M_1, the total number of negatively charged NV centers evolves throughout each stage of the experiment (Appendix B), depending on the presence or absence of optical excitation. As a consequence, the measured PL signal can be interpreted as the product of the intrinsic population dynamics expressed in the rate-equation model and a time-dependent modulation associated with the charge-state conversion.

Therefore, fitting the experimental data to Equation 5.2 allows us to extract not only the dominant eigenvalues of the system, but also the back-conversion relaxation rate k_{bc}, which governs the recombination dynamics and determines how the NV^- population decreases after a given time in the dark.

5.2.3 Matrices and Eigenvalues

The matrices that describe the evolution of the populations are bellow. M_0 is responsible for the laser-on configuration :

$$M_0 = \begin{bmatrix} -(a+2k_s) & k_s & k_s & k & 0 & 0 & k_{51} & k_{ion} \\ k_s & -(a+k_s) & 0 & 0 & k & 0 & k_{52}/2 & k_{ion} \\ k_s & 0 & -(a+k_s) & 0 & 0 & k & k_{52}/2 & k_{ion} \\ a & 0 & 0 & -(k+k_{35}+a_{ion}) & 0 & 0 & 0 & 0 \\ 0 & a & 0 & 0 & -(k+k_{45}+a_{ion}) & 0 & 0 & 0 \\ 0 & 0 & a & 0 & 0 & -(k+k_{45}+a_{ion}) & 0 & 0 \\ 0 & 0 & 0 & k_{35} & k_{45} & k_{45} & -(k_{51}+k_{52}) & 0 \\ 0 & 0 & 0 & a_{ion} & a_{ion} & a_{ion} & 0 & -3k_{ion} \end{bmatrix} \tag{5.3}$$

And, for the laser-off configuration,

$$M_1 = \begin{bmatrix} -2k_s & k_s & k_s & k & 0 & 0 & k_{51} & k_{ion} \\ k_s & -k_s & 0 & 0 & k & 0 & k_{52}/2 & k_{ion} \\ k_s & 0 & -k_s & 0 & 0 & k & k_{52}/2 & k_{ion} \\ 0 & 0 & 0 & -(k+k_{35}) & 0 & 0 & 0 & 0 \\ 0 & 0 & 0 & 0 & -(k+k_{45}) & 0 & 0 & 0 \\ 0 & 0 & 0 & 0 & 0 & -(k+k_{45}) & 0 & 0 \\ 0 & 0 & 0 & k_{35} & k_{45} & k_{45} & -(k_{51}+k_{52}) & 0 \\ 0 & 0 & 0 & 0 & 0 & 0 & 0 & -3k_{ion} \end{bmatrix} \tag{5.4}$$

One important detail is that spin-flip transitions are not considered. These transitions are at most 2% of the spin conserving counterparts as reported by (Robledo *et al.*, 2011) and their rates are taken as zero. For instance, the transitions $P_{2m} \rightarrow P_{4p}$ or $P_3 \rightarrow P_{2p}$ are not possible in our model.

with eigenvalues listed bellow:

Table 9 – Eigenvalues of the M_1 matrix defined in Equation 5.4.

Eigenvalue	Multiplicity
0	1
$-(k + k_{35})$	1
$-(k + k_{45})$	2
$-k_s$	1
$-3k_s$	1
$-(k_{51} + k_{52})$	1
$-3k_{ion}$	1

(Calculated with SymPy)

The eigenvalue associated with the increase in the PL signal around 4 μs is $-3k_{ion}$, which is directly related to the recombination dynamics following ionization. Since ionization converts NV^- into NV^0, the subsequent relaxation through tunneling transitions (as represented in Figure 6) leads to a recovery of the NV^- population after a dark time.

The variation in the NV^- population due to back-conversion and its associated relaxation is described by two functions. The function $\mathcal{N}_{on}(t)$ accounts for the laser-driven conversion of NV^0 into NV^- during an excitation pulse of duration t:

$$\boxed{\mathcal{N}_{on}(N_{in}, t) = N_{max} - (N_{max} - N_{in})\, e^{-(a_{bc}t)^m}}. \tag{5.5}$$

This function maps the initial number of negatively charged NV centers, N_{in}, to a maximum saturation value N_{max} as $t \rightarrow \infty$, with a characteristic conversion rate a_{bc}.

In the absence of laser excitation, the system relaxes in the opposite direction, partially recovering the NV^0 population. Starting from an initial NV^- population N'_{in}, the system evolves toward an equilibrium value N_{min} after a dark time τ, governed by a relaxation rate k_{bc}. The corresponding function is given by:

$$\boxed{\mathcal{N}_{off}(N'_{in}, \tau) = N_{min} + (N'_{in} - N_{min})\, e^{-(k_{bc}\tau)^n}}. \tag{5.6}$$

5.3 Model Fitting and Parameter Extraction

Now we are able to fit our experimental data and associate the extracted parameters to every significant quantity for our PL. The expression used for the fit is given by:

$$PL_{SE}(\tau) = I_{eq}\left(1 + A_{bc}e^{-(k_{bc}\tau)^n}\right)\left(1 + A_1\, e^{\lambda_1\tau} + A_2\, e^{\lambda_2\tau} + A_3\, e^{\lambda_3\tau}\right) \tag{5.7}$$

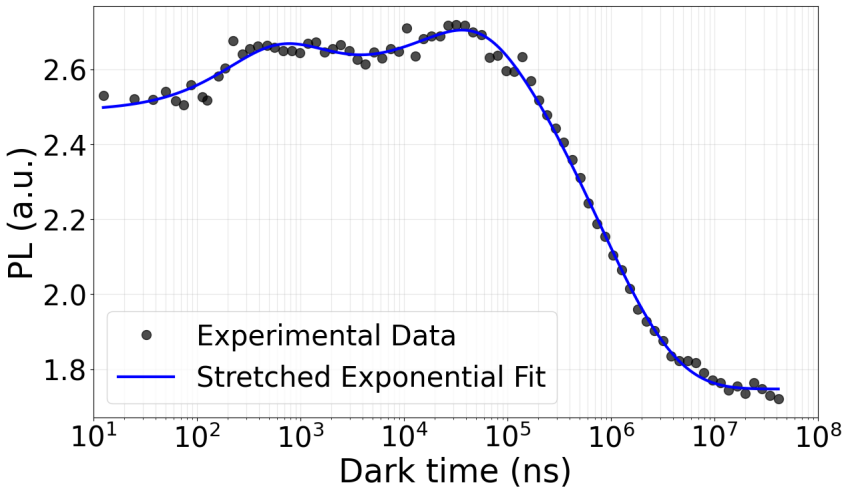

Figure 23 – Stretched exponential model fit for $PL_{initial}$ found in Figure 17. It fits the expression in Equation 5.7.

Table 10 – Stretched exponential fit parameters and corresponding characteristic times ($\tau_i = 1/|\lambda_i|$) for the PL curve in Figure 23.

Mode	A_i	λ_i (numerical, ns^{-1})	τ_i (ns)	λ_i (analytical)
1	-0.082	-4.02×10^{-3}	249	$-(k_{51} + k_{52})$
2	0.032	-7.33×10^{-4}	1.365×10^3	$-3k_s$
3	-0.112	-4.29×10^{-5}	2.33×10^4	$-3k_{ion}$
$A_{bc} = 0.698$	$k_{bc} = 1.32 \times 10^{-6}\,\text{ns}^{-1}$	$T_r = 1/k_{bc} = 7.59 \times 10^5\,\text{ns}$	$n = 0.5713$	
$I_{eq} = 1.7471$				

The values reported in Table 10 exhibit discrepancies when compared to those found in the literature, particularly for the longitudinal relaxation time $T_1 = 1/3k_s$, which is typically on the order of milliseconds for ensemble samples (Doherty *et al.*, 2013). In addition, the characteristic time associated with relaxation from ionization has been reported to be $\sim 100\,\mu s$ in (Giri *et al.*, 2018), while (Gorrini *et al.*, 2021) indicates that recombination from back-conversion occurs on timescales exceeding 10 ms.

In contrast, only the timescale associated with decay through the metastable channel, ~ 200 ns, is consistent with values reported in the literature. These discrepancies indicate that the extracted parameters should be interpreted as effective rates. As discussed in chapter 6, using these parameters as inputs to the model allows us to reproduce the PL curve shown in Figure 23.

Since the extracted time scales deviate from the expected values for $3k_s$ and $3k_{ion}$, each exponential contribution was identified based on the sign of its amplitude. Recharge from the ionization process leads to an increase in the PL signal; therefore, the corresponding exponential term must have a negative amplitude. On the other hand, longitudinal spin relaxation results in a decrease of the PL signal, implying a positive amplitude for the associated exponential contribution.

5.3.1 Emission Decay Experiment Fit

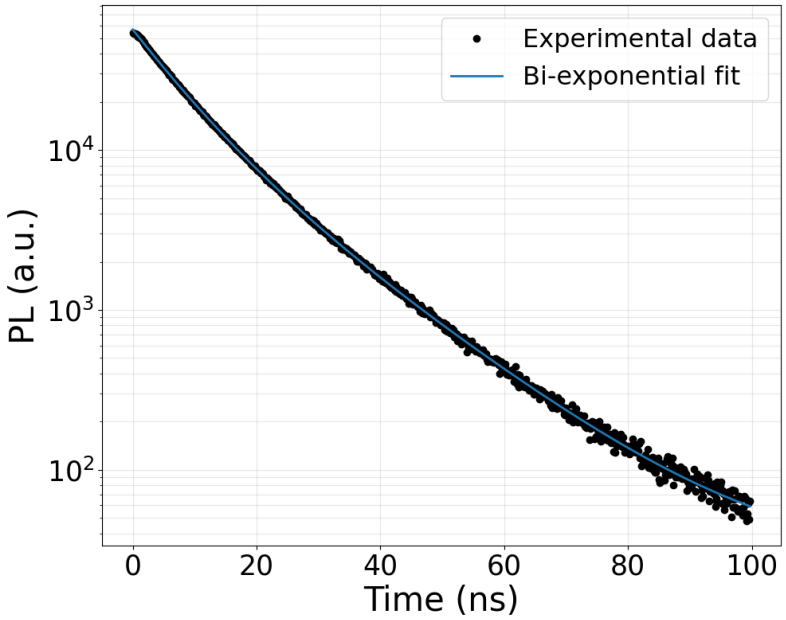

Figure 24 – Bi-exponential fit for the emission decay curve of DNV-B14.

Table 11 – Fit parameters and corresponding characteristic times ($\tau_i = 1/|\lambda_i|$) for the emission decay experiment.

Spin state	A_i	τ_i (ns)	λ_i (ns^{-1})	λ_i
$m_s = 0$	635.2157	15.6	6.4×10^{-2}	$-(k + k_{35})$
$m_s = \pm 1$	1353.1834	7.4	1.36×10^{-1}	$-(k + k_{45})$
		C = 28.5		

The two remaining eigenvalues needed to complete our model can be found above through a bi-exponential fit of the emission decay curve,

$$R(t) = k\left[P_3(t) + P_{4m}(t) + P_{4p}(t)\right],$$

as discussed in section 3.3.

6 Simulation Results

Utilizing the matrices defined in Equation 5.3 and Equation 5.4, the internal dynamics of the NV center can be described through the differential equation

$$\frac{d\vec{P}}{dt} = M\vec{P}, \tag{6.1}$$

while the evolution of the negatively charged population NV^- is independently tracked by the functions introduced in Equation 5.5 and Equation 5.6.

The emission rate at a given time t can be expressed as

$$R(t) = k\, N^-(t)\, [P_3(t) + P_{4m}(t) + P_{4p}(t)]\,, \tag{6.2}$$

where $N^-(t)$ denotes the population of NV centers in the negative charge state, and $P_i(t)$ represents the population of the i-th energy level at time t.

The photoluminescence for our stretched-exponential model is obtained by integrating the emission rate over the detection window of duration T_{DW}. The integrated photoluminescence as a function of the dark time τ is given by

$$\mathrm{PL}_{SE}(\tau) = \int_0^{T_{DW}} R(t,\tau)\, dt. \tag{6.3}$$

This formulation follows the same procedure adopted in chapter 5 to simulate the photoluminescence, now incorporating the specific matrices and definitions of the stretched-exponential model. Now it becomes possible to reproduce the $PL_{initial}$ behavior observed experimentally, as shown in Figure 25.

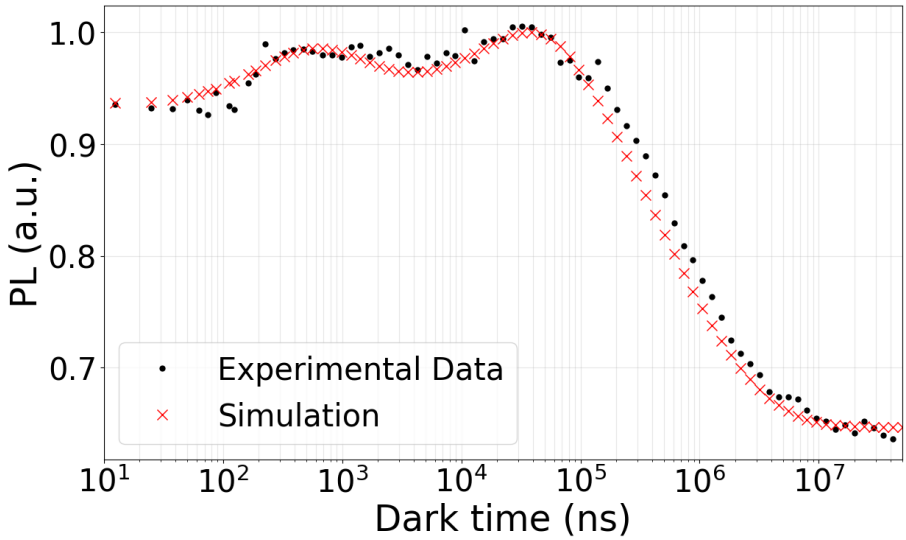

Figure 25 – Simulation of $PL_{initial}$ using the stretched exponential model. The photoluminescence is normalized such that its maximum value is equal to 1.

To perform this simulation, it is necessary to estimate the transition rates from the eigenvalues. While the experiments provide access to the eigenvalues of the matrix M_1, they do not directly yield the individual transition rates associated with them.

In addition, the model requires a set of free parameters, particularly those related to laser-driven processes, such as a and a_{ion}. The considerations that guided the selection of these parameters are discussed in the following sections.

The transition rates, stretching factors and free parameters utilized in the simulation from Figure 25 are in Table 12.

Table 12 – Transition rates, stretching factor and free parameters used in Figure 25.

Transition Rates (ns^{-1})		**Free Parameters**	
Rate	Value	Parameter	Value
k	0.0493	a	0.00685 ns^{-1}
k_s	2.44×10^{-4}	N_{max}	1.78
k_{bc}	1.32×10^{-6}	m	0.57
k_{ion}	1.43×10^{-5}	a_{bc}	1.32×10^{-6} ns^{-1}
k_{35}	0.0147	a_{ion}	1.87×10^{-4} ns^{-1}
k_{45}	0.0863		
k_{51}	1.34×10^{-3}		
k_{52}	2.68×10^{-3}		

$$\boxed{n = 0.57} \tag{6.4}$$

Stretching exponential

6.1 Free Parameters

6.1.0.1 The parameter a

As mentioned previously, the simulation presented in Figure 25 requires the introduction of a set of free parameters. The first of these is the parameter a, which is associated with the laser excitation power and governs the transitions from the ${}^3A_2$ ground state to the ${}^3E$ excited-state manifold.

This parameter is known to be proportional to k, the radiative decay rate for spin-conserving transitions between ${}^3E$ and ${}^3A_2$ (Tetienne; Rondin, *et al.*, 2012). In this work, however, a is treated as an independent rate, rather than being expressed as σk, where σ represents the proportionality factor related to the laser excitation power. This choice ensures consistency in notation, as a, a_{ion}, and a_{bc} are all associated with laser-driven processes.

The parameter a has been considered since the first model provided by (Song *et al.*, 2020) and is expected to scale with the laser power. However, a variation in laser power also

affect other parameters, such as a_{ion} and a_{bc}, which makes it necessary to adopt a dedicated procedure to determine a value of a that adequately represents the experimental conditions of our setup. In the present simulations, variations in a primarily influence the initial photoluminescence level, corresponding to the first data point (dark time $\tau = 12.5\,\text{ns}$).

6.1.0.2 The parameter a_{ion}

The parameter a_{ion}, introduced in section 3.4, accounts for the ionization process under laser excitation. Both the ionization rate a_{ion} and the recombination rate k_{ion} are known to exhibit a quadratic dependence on the excitation power (Aslam *et al.*, 2013). This dependence suggests that a_{ion} can be expressed in the form $a_{\text{ion}} = \sigma_{\text{ion}} k_{\text{ion}}$, where σ_{ion} captures the effect of the optical excitation. In addition, it has been reported that both ionization and recombination rates depend on the wavelength of the excitation laser (Aslam *et al.*, 2013; Chen *et al.*, 2013). For the purpose of sample characterization, a detailed treatment of a_{ion} is beyond the scope of this work.

In the simulations, variations in a_{ion} primarily affect the shape of the photoluminescence curve, particularly the amplitude of the peak located around $4 \times 10^5\,\text{ns}$ and its relative contrast with respect to the shorter-time features of the signal, like the local peak around $250\,ns$.

6.1.0.3 The parameter N_{max}

The parameter N_{max} naturally arises from the formulation introduced in Equation 5.5 and represents the saturation limit for the population of negatively charged NV centers. Physically, it corresponds to the maximum gain of NV^- that can be generated under continuous laser excitation, beyond which no further conversion from NV^0 occurs.

The modeling of this process is that NV^- is converted from NV^0 via two-photon absorption which inherently limits the achievable NV^- population. Moreover, the system is governed by the interplay between ionization and back-conversion mechanisms, which, after sufficient illumination time, lead to a steady-state condition where the populations of NV^- and NV^0 remain constant.

The back-conversion is dependent on the density of NV^0 in the sample. In (Gorrini *et al.*, 2021) they use shallow NV samples specially because the surface effects tends to favor the occurrence of NV^0 over its photoactive negative charged counterpart. For the sample used in this work, the NV^0 density is neither specified in the datasheet (Element Six, 2021) nor independently characterized in our laboratory. Thus, the relation between these characteristics of our sample and the parameter N_{max} could be studied in future work.

This parameter is important for the charge dynamics associated to back-conversion with laser-on configuration. Variations in this parameter primarily affect the difference

between the initial PL signal (dark time $\tau = 12.5\,\text{ns}$) and the long-time behavior (dark time $\tau > 10\,\text{ms}$).

The simulation presented in Figure 25 utilizes $N_{max} = 1.78$ and the minimum is taken to be equal to 1. This means the sample is able to have a gain of 78% of NV^- caused by the conversion $NV^0 \rightarrow NV^-$. This high gain in NV^- is also observed in Figure 21.

6.1.0.4 The parameters a_{bc} and m

The parameters a_{bc} and m are associated with the modeling of the back-conversion process under laser excitation. In particular, m is the stretching factor of the exponential function and controls how sharply the transition from unity to zero occurs. Although this parameter is not extensively discussed in the main reference (Gorrini *et al.*, 2021), it plays a relevant role in shaping the temporal response of the charge dynamics.

As observed by (Gorrini *et al.*, 2021) in their fit for Figure 21, the value of m tends to approach unity for lower excitation powers. However, the experimentally observed population dynamics suggest a sharper transition, consistent with values closer to $m \sim 0.5$. In the present work, m is set equal to the fitted parameter n for simplicity. A more rigorous treatment of m, together with a_{bc}, would require a detailed analysis of the dynamics under continuous laser excitation, which is beyond the scope of this study.

The rate a_{bc} sets the characteristic timescale for the back-conversion process. Higher values of a_{bc} lead to a faster approach to the saturation population N_{max}.

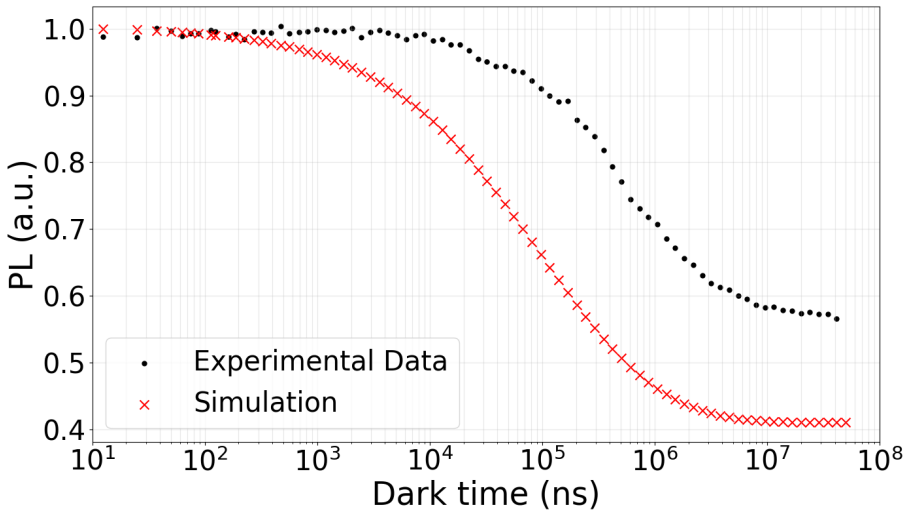

Figure 26 – Simulated PL_{final} obtained with the stretched exponential model. The photoluminescence is normalized to its maximum value.

Although the model reproduces the photoluminescence behavior in the dark, as observed in Figure 25, it fails to accurately describe the dynamics under laser excitation for the parameters listed in Table 12. This discrepancy becomes evident in the simulation of PL_{final}, shown in Figure 26.

This result indicates that the chosen parameters do not fully capture the behavior of the sample during laser illumination. A more detailed inspection of the photon emission during the probe pulse of 500 μs reveals the complexity of the dynamics in the presence of laser excitation.

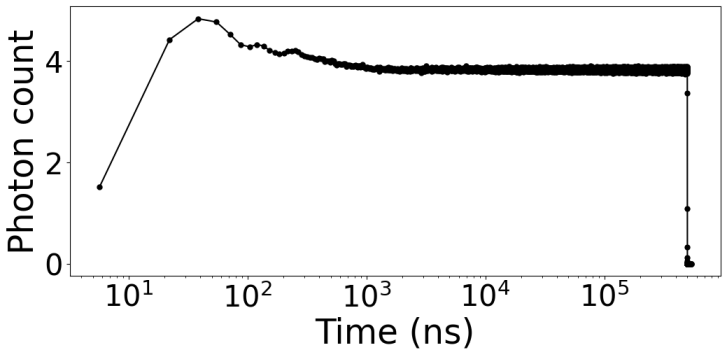

(a) Photon count after a dark time of 1 μs.

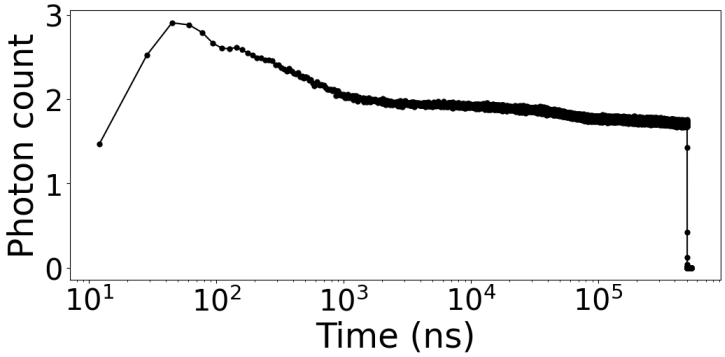

(b) Photon count after a dark time of 10 ms.

Figure 27 – Photon count recorded during the probe pulse for two different dark times. In (a), the dark time is 1 μs, while in (b) it is 10 ms. The photon count is scaled by a factor of 10^4.

The integration of the photon counts in Figure 27(a) over the first 1 μs and the last 1 μs of the pulse yields the PL values associated with $\tau = 1$ μs in Figure 17 and Figure 18, respectively. The same procedure applies to Figure 27(b).

The two cases presented in Figure 27 exhibit different behaviors. For shorter dark times, in (a), the contrast between the initial emission peak and the saturation level is reduced, and the photon counts remain approximately constant around 4×10^4 after 1 μs of dark time. In contrast, for longer dark times, as in (b), the system requires nearly the entire duration of the probe pulse (500 μs) to approach saturation. This behavior may not be evident without the use of a logarithmic time scale. In fact, 500 μs is not sufficient to fully saturate the system under these conditions.

The discrepancy between simulation and experiment in the presence of laser excitation becomes even more evident when directly comparing the temporal emission profiles:

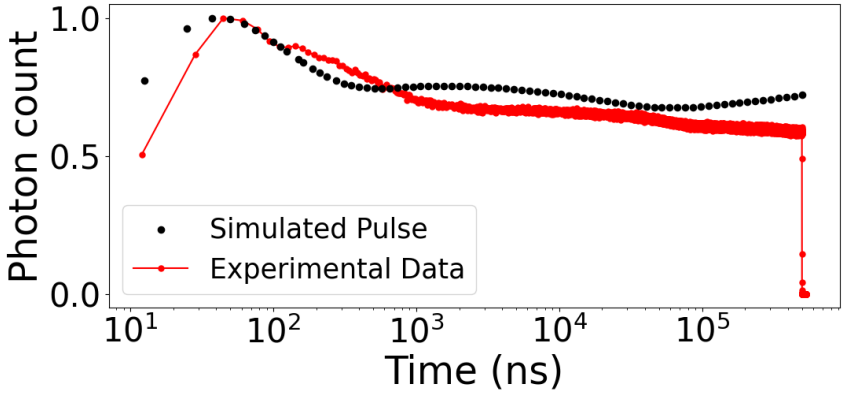

Figure 28 – Comparison between experimental and simulated emission during a probe pulse of 500 μs. Both signals are normalized by their maximum photon count.

Comparing both profiles, the model reproduces the initial peak and the intermediate smooth hump, albeit with different characteristic time scales. However, a significant discrepancy arises for times longer than 10^5 ns, where the model predicts an increasing trend in the photon emission, in contrast to the behavior observed experimentally.

Although the available evidence suggests that a_{bc} is a slow rate, an additional simulation was performed assuming a faster value, yielding important results.

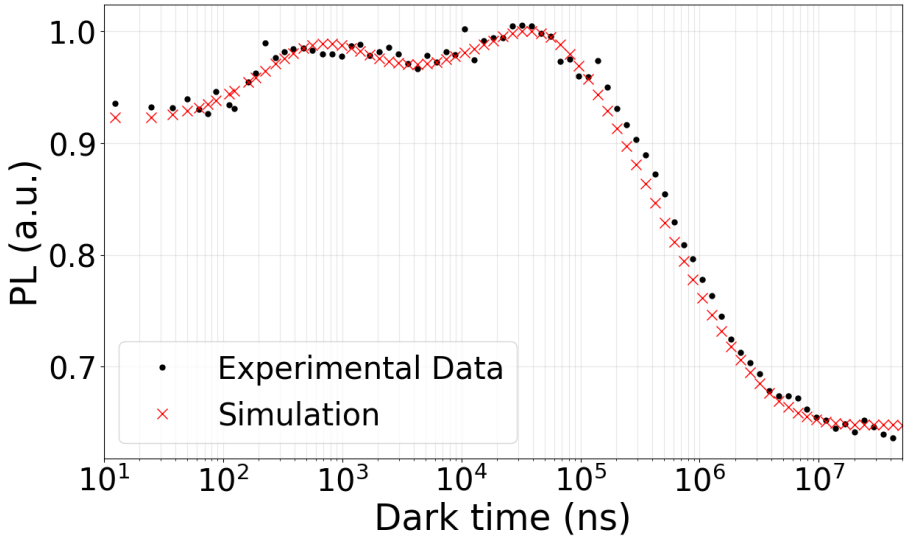

Figure 29 – Simulation of $PL_{initial}$ using the stretched exponential model with an increased a_{bc}. The photoluminescence is normalized such that its maximum value is equal to 1. The corresponding parameters and transition rates are listed in Table 13.

The simulation presented in Figure 29 produces a PL profile very similar to that of Figure 25. This is expected, as the overall shape of this curve is predominantly governed by the dark dynamics, which are well captured by the model.

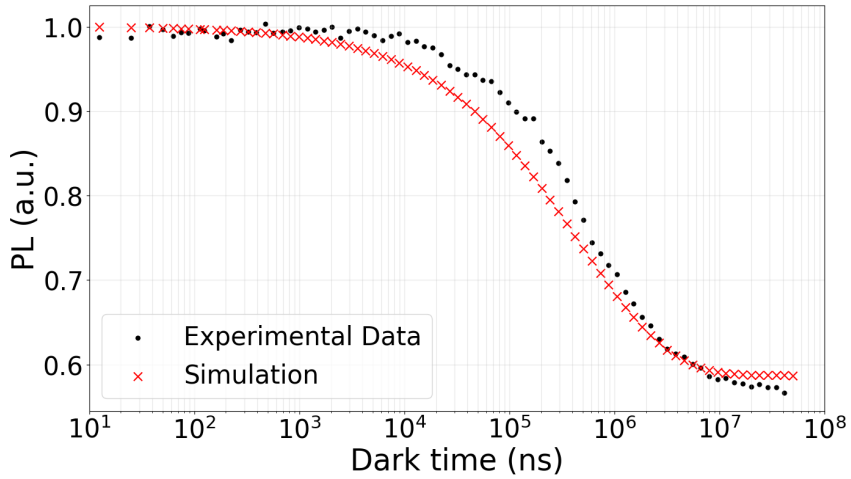

Figure 30 – Simulated PL_{final} obtained with the stretched exponential model using an increased a_{bc}. The photoluminescence is normalized to its maximum value. The corresponding parameters and transition rates are listed in Table 13.

The simulations involving laser excitation show improved agreement when assuming $a_{bc} = 0.04$. As shown in Figure 30, the decay profile of the simulated PL becomes more consistent with the experimental data when compared to the results obtained with the parameters in Table 12.

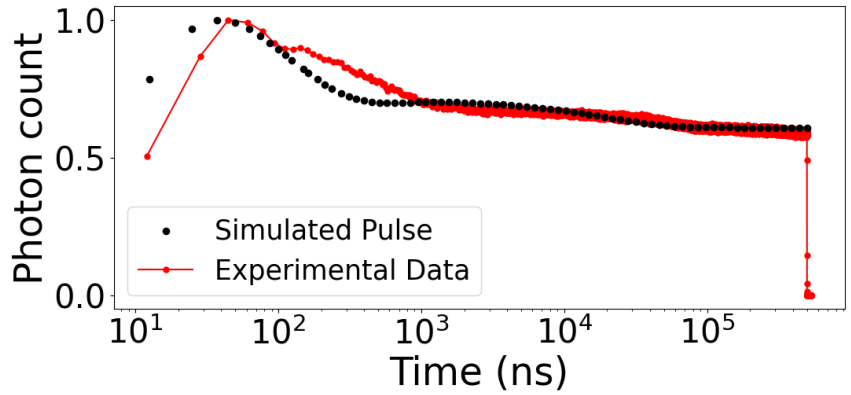

Figure 31 – Comparison between experimental and simulated emission during a probe pulse of 500 μs using an increased a_{bc}. Both signals are normalized by their maximum photon count. The corresponding parameters and transition rates are listed in Table 13.

The simulation of the photon emission during laser excitation also shows a clear improvement. In Figure 31, the artificial increase in emission around 10^5 ns is no longer observed, and the intermediate hump is more accurately reproduced. However, the model still fails to capture the behavior in the time range between $10^2\,ns$ and $10^3\,ns$.

Despite these improvements, it has been consistently argued throughout this work that a_{bc} should correspond to a slower process. These results therefore highlight the need for a dedicated investigation of the charge dynamics under laser excitation in order to fully understand the mechanisms and develop a more accurate model.

Table 13 – Transition rates and free parameters used in Figure 25, Figure 30 and Figure 31.

Transition Rates (ns^{-1})		**Free Parameters**	
Rate	Value	Parameter	Value
k	0.0493	a	0.0079 ns^{-1}
k_s	2.44×10^{-4}	N_{max}	1.91
k_{bc}	1.32×10^{-6}	m	0.57
k_{ion}	1.43×10^{-5}	a_{bc}	0.04 ns^{-1}
k_{35}	0.0147	a_{ion}	1.5×10^{-4} ns^{-1}
k_{45}	0.0863		
k_{51}	1.34×10^{-3}		
k_{52}	2.68×10^{-3}		

Stretching exponential:

$$n = 0.57$$

6.2 Estimating Transition Rates

Some eigenvalues of the matrix M_1, which governs the electronic dynamics in the dark, are associated with more than one transition rate. Since experimental procedures provide access only to these eigenvalues, determining the corresponding transition rates is a important step in the construction of the model.

Although the photoluminescence is ultimately governed by the eigenvalues of M_1, an inappropriate choice of the transition rates can lead to unphysical population dynamics and, consequently, to unrealistic PL curves, as will be illustrated in this section.

First, to estimate k , k_{35} and k_{45} from the eigenvalues summarized in Table 11 it was employed the following system of equations:

$$\begin{aligned} 6.4 \times 10^{-2} &= k + k_{35} \\ 1.36 \times 10^{-1} &= k + k_{45} \\ 0.17 &= k_{35}/k_{45} \end{aligned} \tag{6.5}$$

The ratio k_{35}/k_{45} is taken from (Song *et al.*, 2020) and (Tetienne; Rondin, *et al.*, 2012). This choice ensures that the relative contribution of non-radiative decay from the $m_s = 0$ and $m_s = \pm 1$ spin sublevels is consistent with values reported in the literature.

In contrast, the same reasoning cannot be directly applied to the ratio k_{51}/k_{52}, as different works report significantly different values. For instance, (Song *et al.*, 2020) adopts $k_{51}/k_{52} = 1.5$, while (Manson; Harrison; Sellars, 2006) assumes $k_{52} = 0$. Simulations considering both scenarios are shown in Figure 32:

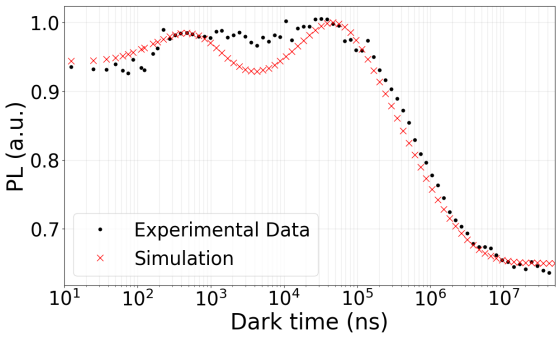

(a) Simulation of the dark-time experiment using $k_{51}/k_{52} = 1.5$, as reported in (Song *et al.*, 2020).

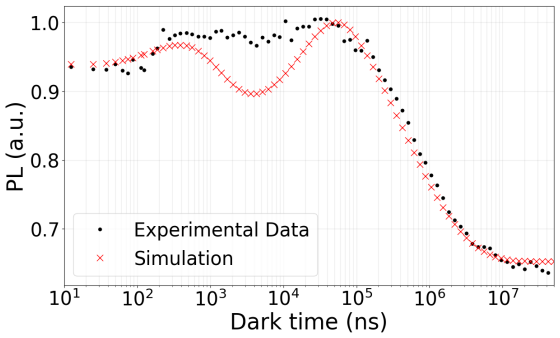

(b) Simulation of the dark-time experiment using $k_{52} = 0$, as reported in (Manson; Harrison; Sellars, 2006).

Figure 32 – Comparison between simulated photoluminescence curves obtained using different assumptions for the ratio k_{51}/k_{52}. Increasing k_{51} implies in a sharp decrease in the PL signal around 4 μs.

Among the tested configurations, the relation reported in (Tetienne; Rondin, *et al.*, 2012) provides the best agreement with the experimental data. In this approach, the decay rates from the excited-state populations P_3, P_{4p}, and P_{4m} to the metastable state P_5 are taken to be equal, leading to the condition $k_{51} = k_{52}/2$.

In the simulations, the ratio between k_{51} and k_{52} directly affects the shape of the photoluminescence curve, particularly the feature around 4 μs. Increasing k_{51} results in a sharper dip in this region. As discussed in (Robledo *et al.*, 2011), both k_{51} and k_{52} exhibit a dependence on temperature, which suggests that the characteristics of this feature in the experimental data may carry information about the ambient conditions of the sample.

7 Conclusion

In this work, a modified rate-equation model was developed to describe the photoluminescence dynamics of a high-density NV ensemble, incorporating both electronic dynamics and charge conversion processes. By combining dark-time and photoemission lifetime experiments, it was possible to extract the eigenvalues of the matrix M_1 and estimate effective transition rates that reproduce the experimental observations with good agreement in the absence of laser excitation.

The extracted transition rates should be interpreted as effective parameters obtained from fits to experimental data. When incorporated into the proposed model, these rates reproduce the observed behavior under specific experimental conditions. However, in some cases, their values differ significantly from those reported in the literature. This indicates that the extracted rates do not correspond to isolated physical processes, but rather represent effective quantities that include contributions from multiple mechanisms.

In addition to the intrinsic complication that arises when measurements are performed on an ensemble of centers, where each center has different local conditions, the assumption that variations in the NV^- population do not affect the internal dynamics of the system is likely a major source of discrepancy between the extracted parameters and literature values.

Despite the success of the model in reproducing the dark-time dynamics, significant discrepancies arise in the presence of laser excitation. In particular, the model fails to fully capture the temporal behavior of the photoluminescence during the probe pulse, as it can be seen in Figure 26 and in Figure 28.

These observations point to several directions for future work. First, more conventional experimental techniques should be employed for the purpose of independent characterization, such as NV lifetime measurements as performed in (Robledo *et al.*, 2011), as well as direct measurements of the longitudinal relaxation time T_1 using microwave-based methods. These experiments would provide independent access to the transition rates, allowing for a more direct comparison with the effective rates extracted from the present model.

Second, the pronounced feature observed in the PL curve around $4\,\mu s$ may be related to temperature-dependent processes, particularly those involving the metastable state and charge dynamics. Investigating the temperature dependence of this feature could provide further insight into the mechanisms governing the system and potentially enable the use of this signal as a probe of local thermal conditions.

The incorporation of the internal dynamics of NV^0 into the model could provide a more comprehensive description of the system and generate more accurate simulations. This extension would allow for explicit transitions between the ground and excited states

of NV^0, as well as enable NV^0 centers, generated through the ionization of NV^-, to convert back to NV^0 through back-conversion via two-photon absorption.

Another important aspect concerns the maximum achievable NV^- population, an its relation to the parameter N_{max}. A more detailed analysis of this quantity, and its relation to the density of NV^0 centers in the sample, would improve the understanding of the charge conversion processes under laser excitation.

Additionally, spatial inhomogeneities in the sample were not considered in the present model. The measured photoluminescence may depend on the specific region of the sample being probed, especially due to surface effects that can favor the presence of NV^0 as reported by (Gorrini *et al.*, 2021). Since back-conversion is expected to be more significant near the surface, the spatial dependence of the PL curve could substantially improve our model.

This work provides qualitative insights into the investigated sample, and highlights the importance of extending the analysis to samples with different properties such as NV and nitrogen densities, as well as varied fabrication methods. One of these experimental observations is the existence of an optimal dark time for maximum photoluminescence, occurring at approximately 250 ns as observed in Figure 19. This result is directly relevant for optimizing experimental protocols involving the DNV-B14 sample.

The photonic emission observed during the probe pulse for different dark times (Figure 27) and the non-monotonic behavior of the PL curve that includes intermediate dips and and peaks of the signal are clear signatures of charge conversion processes and that the sample may be suitable for techniques based on charge readout, such as photoelectric detection of magnetic resonance (PDMR) (Bourgeois; Gulka; Nesladek, 2020), where charge conversion plays a central role. In summary, the approach developed in this work provides a practical method for the simulation of NV ensembles electronic and charge dynamics based on photoluminescence measurements. While the model successfully captures the dark dynamics and identifies key physical processes, its limitations under laser excitation highlight the need for a deeper investigation of charge dynamics and their interplay with optical excitation. Addressing these challenges represents an important step toward the development of predictive models and applications of NV-based quantum technologies.

References

ASLAM, N.; WALDHERR, G.; NEUMANN, P.; JELEZKO, F.; WRACHTRUP, J. Photo-induced ionization dynamics of the nitrogen vacancy defect in diamond investigated by single-shot charge state detection. **New Journal of Physics**, v. 15, n. 1, p. 013064, 2013. Cit. on pp. 20, 23, 37, 54.

BALASUBRAMANIAN, G.; NEUMANN, P.; TWITCHEN, D.; MARKHAM, M.; EPSKAMP, R.; MIZUOCHI, N.; ISOYA, J.; JELEZKO, F.; WRACHTRUP, J. Ultralong spin coherence time in isotopically engineered diamond. **Nature Materials**, v. 8, n. 5, p. 383–387, 2009. Cit. on p. 16.

BEHA, K.; BATALOV, A.; MANSON, N. B.; BRATSCHITSCH, R.; LEITENSTORFER, A. Optimum Photoluminescence Excitation and Recharging Cycle of Single Nitrogen-Vacancy Centers in Ultrapure Diamond. **Physical Review Letters**, v. 98, n. 045401, 2012. Cit. on p. 15.

BERBERAN-SANTOS, M. N.; MARTINHO, J. M. G. The integration of kinetic rate equations by matrix methods. **Journal of Chemical Education**, v. 67, n. 375, 5 1990. Cit. on pp. 29, 71.

BOURGEOIS, Emilie; GULKA, Michal; NESLADEK, Milos. Photoelectric Detection and Quantum Readout of Nitrogen-Vacancy Center Spin States in Diamond. **Advanced Otpical Materials**, v. 8, n. 1902132, 12 2020. Cit. on pp. 15, 62.

CARBERY, William P.; FARFAN, Camille A.; ULBRICHT, Ronald; TURNER, Daniel B. The phonon-modulated Jahn–Teller distortion of the nitrogen vacancy center in diamond. **Nature Communications**, v. 15, n. 8646, 2024. Cit. on p. 18.

CHEN, Xiang-Dong; ZOU, Chang-Ling; SUN, Fang-Wen; GUO, Guang-Can. Optical manipulation of the charge state of nitrogen-vacancy center in diamond. **Applied Physics Letters**, v. 103, n. 1, p. 013112, 2013. DOI: `10.1063/1.4813120`. Cit. on p. 54.

DOHERTY, Marcus W.; MANSON, Neil B.; DELANEY, Paul; JELEZKO, Fedor; WRACHTRUPE, J.; HOLLENBERG, Lloyd C.L. The nitrogen-vacancy colour centre in diamond. **Physics Reports**, v. 528, p. 1–45, 1 2013. Cit. on pp. 14, 18, 20, 50.

ELEMENT SIX. **DNV Series: DNV B1 and DNV B14 – Unlocking Next Generation Quantum Technologies**. [*S. l.*], 2021. Accessed: 5 Mar 2026. Disponível em: `https://e6cvd.com/media/catalog/category/DNV_B1_B14_datasheet_EN_17.09.21_1.pdf`. Cit. on pp. 38, 54.

FU, Kai-Mei C.; SANTORI, Charles; BARCLAY, Paul E.; ROGERS, Lachlan J.; MANSON, Neil B.; BEAUSOLEIL, Raymond G. Observation of the Dynamic Jahn-Teller Effect in the Excited States of Nitrogen-Vacancy Centers in Diamond. **Physical Review Letters**, v. 103, p. 256404, 25 2009. Cit. on p. 25.

GILARDONI, Carmem M. **Optically addressable spins in silicon carbide and related 2D materials: the effect of symmetry and spin-orbit coupling**. 2021. PhD thesis – University of Groningen. DOI: 10.33612/diss.192999111. Cit. on p. 17.

GIRI, R.; GORRINI, F.; DORIGONI1, C.; AVALOS, C. E.; CAZZANELLI, M.; TAMBALO, S.; BIFONE, A. Coupled charge and spin dynamics in high-density ensembles of nitrogen-vacancy centers in diamond. **Physical Review B**, v. 98, n. 045401, 2018. Cit. on pp. 15, 24, 34–36, 44, 50.

GORRINI, Federico; DORIGONI, Carla; OLIVARES-POSTIGO, Domingo; GIRI, Rakshyakar; APRÀ, Pietro; PICOLLO, Federico; BIFONE, Angelo. Long-Lived Ensembles of Shallow NV– Centers in Flat and Nanostructured Diamonds by Photoconversion. **ACS Applied Materials and Interfaces**, v. 13, p. 43221–43232, 36 2021. Cit. on pp. 22, 24, 41, 44–46, 50, 54, 55, 62.

HINCKS, Ian; GRANADE, Christopher; CORY, David G. Statistical inference with quantum measurements: methodologies for nitrogen vacancy centers in diamond. **New Journal of Physics**, v. 15, n. 1, p. 013064, 2013. Cit. on p. 25.

MAGALETTI, Simone; MAYER, Ludovic; ROCH, Jean-François; DEBUISSCHERT, Thierry. Modelling Rabi oscillations for widefield radiofrequency imaging in nitrogen-vacancy centers in diamond. **New Journal of Physics**, v. 26, 2024. Cit. on p. 29.

MANSON, N. B.; HARRISON, J. P.; SELLARS, M. J. Nitrogen-vacancy center in diamond: Model of the electronic structure and associated dynamics. **Physical Review B**, v. 74, p. 104303, 10 2006. Cit. on pp. 59, 60.

MIZUOCHI, N.; NEUMANN, P.; REMPP, F.; BECK, J.; JACQUES, V.; SIYUSHEV, P.; NAKAMURA, K.; TWITCHEN, D. J.; WATANABE, H.; YAMASAKI, S.; JELEZKO, F.; WRACHTRUP, J. Coherence of single spins coupled to a nuclear spin bath of varying density. **Physical Review B**, v. 80, p. 041201, 4 2009. Cit. on p. 22.

NEUMANN, P.; JAKOBI, I.; DOLDE, F.; BURK, C.; REUTER, R.; WALDHERR, G.; HONERT, J.; WOLF, T.; BRUNNER, A.; WRACHTRUP, J. High precision nano scale temperature sensing using single defects in diamond. **Nano Letters**, v. 13, 6 2013. Cit. on p. 15.

PENFOLD, Thomas J.; GINDENSPERGER, Etienne; DANIEL, Chantal; MARIAN, Christel M. Spin-Vibronic Mechanism for Intersystem Crossing. **Chemical Reviews**, v. 118, p. 6975–7025, 15 2018. Cit. on p. 21.

PEZZAGNA, S.; NAYDENOV, B.; JELEZKO, F.; WRACHTRUP, J.; MEIJER, J. Creation efficiency of nitrogen-vacancy centres in diamond. **New Journal of Physics**, v. 12, n. 6, p. 065017, 2010. Cit. on p. 16.

PHAM, L. M.; BAR-GILL, N.; LE SAGE, D.; BELTHANGADY, C.; STACEY, A.; MARKHAM, M.; TWITCHEN, D. J.; LUKIN, M. D.; WALSWORTH, R. L. Enhanced metrology using preferential orientation of nitrogen-vacancy centers in diamond. **Physical Review B**, v. 86, 12 2012. Cit. on p. 17.

POGGIALI, F.; CAPPELLARO, P.; FABBRI, N. Measurement of the excited-state transverse hyperfine coupling in NV centers via dynamic nuclear polarization. **Physical Review B**, v. 95, p. 195308, 19 2017. Cit. on p. 25.

REMBOLD, Phila; OSHNIK, Nimba; MÜLLER, Matthias M.; MONTANGERO, Simone; CALARCO, Tommaso; NEU, Elke. Introduction to quantum optimal control for quantum sensing with nitrogen-vacancy centers in diamond. **AVS Quantum Sci.**, v. 2, n. 024701, 2 2020. Cit. on pp. 14, 19, 21.

ROBLEDO, Lucio; BERNIEN, Hannes; SAR, Toeno van der; HANSON, Ronald. Spin dynamics in the optical cycle of single nitrogen-vacancy centres in diamond. **New Journal of Physics**, v. 13, n. 2, p. 025013, 2011. Cit. on pp. 20, 49, 60, 61.

ROGERS, L. J.; MCMURTRIE, R.L.; SELLARS, M. J.; MANSON, N. B. Time-averaging within the excited state of the nitrogen-vacancy centre in diamond. **New Journal of Physics**, v. 11, n. 6, p. 063007, 2009. Cit. on p. 25.

RONDIN, L.; TETIENNE, J.-P; HINGANT, T.; ROCH, J.-F.; MALETINSKY, P.; JACQUES, V. Magnetometry with nitrogen-vacancy defects in diamond. **Reports on Progress in Physics**, v. 77, n. 056503, 2014. Cit. on p. 14.

SHIELDS, B. J.; UNTERREITHMEIER, Q. P.; LEON, N. P. de; PARK, H.; LUKIN, M. D. Efficient readout of a single spin state in diamond via spin-to-charge conversion. **Physical Review Letters**, v. 114, n. 136402, 2014. Cit. on p. 15.

SIYUSHEV, P.; PINTO, H.; VÖRÖS, M.; GALI, A.; JELEZKO, F.; WRACHTRUP1, J. Optically Controlled Switching of the Charge State of a Single Nitrogen-Vacancy Center in Diamond at Cryogenic Temperatures. **Physical Review Letters**, v. 110, p. 167402, 16 2013. Cit. on pp. 23, 24.

SONG, Yumeng; TIAN, Yu; HU, Zhiyi; ZHOU, Feifei; XING, Tengteng; LU, Dawei; CHEN, Bing; WANG, Ya; XU, Nanyang; DU, Jiangfeng. Pulse-width-induced polarization enhancement of optically pumped N-V electron spin in diamond. **Photonic Research**, v. 8, n. 8, p. 1289–1295, 2020. Cit. on pp. 20, 25–27, 29, 53, 59, 60.

TAYLOR, J. M.; CAPPELLARO, P.; CHILDRESS, L.; JIANG, L.; BUDKE, D.; HEMMER, P. R.; YACOBY, A.; WALSWORTH, R.; LUKIN, M. D. High-sensitivity

diamond magnetometer with nanoscale resolution. **Nature Phys**, v. 4, p. 810–816, 2008. Cit. on p. 14.

TETIENNE, J.-P.; HINGANT, T.; RONDIN, L.; CAVAILLÈS, A.; MAYER, L.; DANTELLE, G.; GACOIN, T.; WRACHTRUP, J.; ROCH, J.-F.; JACQUES, V. Spin relaxometry of single nitrogen-vacancy defects in diamond nanocrystals for magnetic noise sensing. **Physical Review B**, v. 87, n. 23, p. 235436, 2013. Cit. on pp. 22, 27–29, 32.

TETIENNE, J.-P.; RONDIN, L.; CHIPAUX, M.; DEBUISSCHERT, T.; ROCH, J.-F.; JACQUES, V. Magnetic-field-dependent photodynamics of single NV defects in diamond: an application to qualitative all-optical magnetic imaging. **New Journal of Physics**, v. 14, n. 10, p. 103033, 2012. Cit. on pp. 53, 59, 60.

ZAITSEV, A. M. **Optical Properties of Diamond: A Data Handbook**. Berlin, Heidelberg: Springer, 2001. Cit. on p. 16.

Appendix

APPENDIX A – PL expression - rate-equation model

The derivation of the photoluminescence expression is presented for the experiment discussed in section 3.2, considering the 8-level model, although the procedure can be extended to any finite-dimensional system. We assume that the matrix M_0, corresponding to the laser-pumping configuration, is at least numerically diagonalizable. For higher-dimensional systems, an analytical diagonalization may become impractical. In particular, M_0 is more difficult to diagonalize than M_1 because it is less sparse.

On the other hand, diagonalizing M_1 is especially useful, since its eigenvalues are directly related to the experimentally observed decay rates. As will be shown, the PL curve can be written as a sum of exponential terms whose exponents are precisely the eigenvalues of M_1. Therefore, by fitting the experimental PL curve with a multi-exponential model, the extracted decay constants can be directly associated with the eigenvalues of M_1.

The experiment consists of initializing the NV center from the thermal state $\vec{P}_0$ using a 532 nm laser pulse for 500 μs, followed by a dark interval of duration τ (laser off). After this dark time, the laser is turned on again and the photoluminescence (PL) counts are collected during a detection window of 300 ns at the beginning of the probe laser pulse (Figure 10).

We define:

$$\tau = \text{dark time (evolution under } M_1), \qquad t = \text{probe duration (evolution under } M_0).$$

The initialization stage of $t_{\text{init}} = 500\mu s$ is described by

$$\vec{\Psi} = e^{M_0\, t_{\text{init}}}\, \vec{P}_0, \tag{A.1}$$

where the initial thermal state is

$$\vec{P}_0 = \begin{pmatrix} 1/3 \\ 1/3 \\ 1/3 \\ 0 \\ 0 \\ 0 \\ 0 \\ 0 \end{pmatrix}. \tag{A.2}$$

After initialization, the laser is switched off and the system evolves according to the dynamics described by M_1.

Since M_1 is diagonalizable, we can write

$$M_1 = V D_1 V^{-1}, \tag{A.3}$$

where D_1 is the diagonal matrix containing the eigenvalues λ_i of M_1, and the columns of V are the corresponding eigenvectors $\vec{v}_i$ with:

$$M_1\vec{v}_i = \lambda_i\vec{v}_i. \tag{A.4}$$

Thus, after a dark time τ, the initialized state evolves as

$$\vec{\phi}(\tau) = e^{M_1\tau}\vec{\Psi} = Ve^{D_1\tau}V^{-1}\vec{\Psi} = \sum_{i=1}^{n} e^{\lambda_i\tau}\vec{v}_i\left(V^{-1}\vec{\Psi}\right)_i, \tag{A.5}$$

where $\left(V^{-1}\vec{\Psi}\right)_i$ denotes the i-th component of the vector $V^{-1}\vec{\Psi}$.

We also apply the spectral decomposition to M_0 (in our case, numerically diagonalized):

$$M_0 = UD_0U^{-1}, \qquad e^{M_0t} = Ue^{D_0t}U^{-1}, \tag{A.6}$$

where D_0 is the diagonal matrix of eigenvalues α_j of M_0, and the columns of U are the corresponding eigenvectors $\vec{u}_j$, satisfying

$$M_0\vec{u}_j = \alpha_j\vec{u}_j. \tag{A.7}$$

The population vector after $t_{\text{init}} = 500\mu s$ of initialization, a dark time τ, and a probe duration t is

$$\vec{P}(t,\tau) = e^{M_0t}e^{M_1\tau}e^{M_0500\,\mu s}\vec{P}_0 = e^{M_0t}e^{M_1\tau}\vec{\Psi} = e^{M_0t}\vec{\phi}(\tau). \tag{A.8}$$

Using the spectral decomposition for both matrices, the above equation can be written explicitly as

$$\vec{P}(t,\tau) = \sum_{j=1}^{n} e^{\alpha_jt}\vec{u}_j\left[U^{-1}\sum_{i=1}^{n} e^{\lambda_i\tau}\vec{v}_i\left(V^{-1}\vec{\Psi}\right)_i\right]_j. \tag{A.9}$$

In compact matrix form, which is more convenient for numerical implementation in Python, we use

$$\vec{P}(t,\tau) = Ue^{D_0t}U^{-1}Ve^{D_1\tau}V^{-1}\vec{\Psi}. \tag{A.10}$$

The instantaneous emission rate is defined as

$$R(t,\tau) = k_{31}P_3(t,\tau) + k_{42}P_{4m}(t,\tau) + k_{42}P_{4p}(t,\tau). \tag{A.11}$$

Since $k_{31} = k_{42} = k$, this simplifies to

$$R(t,\tau) = k\left[P_3(t,\tau) + P_{4m}(t,\tau) + P_{4p}(t,\tau)\right]. \tag{A.12}$$

Here, $P_3(t,\tau)$, $P_{4m}(t,\tau)$, and $P_{4p}(t,\tau)$ are the components of $\vec{P}(t,\tau)$ corresponding to levels 3, 4_m, and 4_p, respectively.

The photoluminescence signal is obtained by integrating the emission rate over the detection window (in our case, it coincides with the probe duration) $t = 300$ ns:

$$\mathrm{PL}(\tau) = \int_0^{300\,\mathrm{ns}} R(t,\tau)\,dt = \int_0^{300\,\mathrm{ns}} k\,[P_3(t,\tau) + P_{4m}(t,\tau) + P_{4p}(t,\tau)]\,dt. \tag{A.13}$$

Starting from the final population given in Equation A.8 we are able to derive the PL expression with $t_{\mathrm{init}} = 500$ μs and detection window $t = 300$ ns.

For the 8-level model we can define the row vector $\vec{s}^T$ that selects the radiative excited-state populations as:

$$\vec{s}^T = \begin{pmatrix} 0 & 0 & 0 & 1 & 1 & 1 & 0 & 0 \end{pmatrix}. \tag{A.14}$$

we have:

$$\vec{s}^T \vec{P}(t,\tau) = P_3(t,\tau) + P_{4m}(t,\tau) + P_{4p}(t,\tau), \tag{A.15}$$

so that, using $k_{31} = k_{42} = k$ and Equation A.8, the emission is written as

$$R(t,\tau) = k(P_3(t,\tau) + P_{4m}(t,\tau) + P_{4p}(t,\tau)) = k\,\vec{s}^T \vec{P}(t,\tau) = k\,\vec{s}^T e^{M_0 t}\vec{\phi}(\tau). \tag{A.16}$$

The photoluminescence signal in case of a diagonalizable M_0 for any detection window T_{DW}

$$\mathrm{PL}(\tau) = \int_0^{T_{DW}} R(t,\tau)\,dt = k\int_0^{T_{DW}} \vec{s}^T e^{M_0 t}\vec{\phi}(\tau)\,dt = k\int_0^{T_{DW}} \vec{s}^T U e^{D_0 t} U^{-1}\vec{\phi}(\tau)\,dt. \tag{A.17}$$

Let

$$\vec{w}^T \equiv \vec{s}^T U, \qquad \vec{\beta}(\tau) \equiv U^{-1}\vec{\phi}(\tau). \tag{A.18}$$

Since $e^{D_0 t}$ is diagonal, the integral separates:

$$\mathrm{PL}(\tau) = k\sum_{j=1}^{8} w_j\,\beta_j(\tau)\int_0^{T_{DW}} e^{\alpha_j t}\,dt = k\sum_{j=1}^{8} w_j\,\beta_j(\tau)\,F_j(T_{DW}), \tag{A.19}$$

where

$$F_j(T_{DW}) \equiv \int_0^{T_{DW}} e^{\alpha_j t}\,dt = \begin{cases} \dfrac{e^{\alpha_j T_{DW}} - 1}{\alpha_j}, & \alpha_j \neq 0, \\ T_{DW}, & \alpha_j = 0. \end{cases} \tag{A.20}$$

There will be $\alpha_j = 0$ due to NV saturation. When NV is saturated, its state does not change upon more laser excitation, hence $e^{\alpha_j t}\vec{P}_{\mathrm{sat}} = \vec{P}_{\mathrm{sat}}$ and $\vec{P}_{\mathrm{sat}}$ is the eigenstate related to the eigenvalue $\alpha_j = 0$

From Equation A.5

$$\vec{\beta}(\tau) = U^{-1}\vec{\phi}(\tau) = U^{-1} V e^{D_1 \tau} V^{-1}\vec{\Psi}. \tag{A.21}$$

Define $\vec{c} \equiv V^{-1}\vec{\Psi}$, so that $(e^{D_1\tau}\vec{c})_i = e^{\lambda_i\tau}c_i$. Hence,

$$\beta_j(\tau) = \left(U^{-1}Ve^{D_1\tau}\vec{c}\right)_j = \sum_{i=1}^{8}\left(U^{-1}V\right)_{ji} c_i\, e^{\lambda_i\tau}. \tag{A.22}$$

Substituting Equation A.22 into Equation A.19 yields

$$\begin{aligned}\mathrm{PL}(\tau) &= k\sum_{j=1}^{8} w_j\, F_j(T_{DW}) \sum_{i=1}^{8}\left(U^{-1}V\right)_{ji} c_i\, e^{\lambda_i\tau} \\ &= \sum_{i=1}^{8} \underbrace{\left[k\, c_i \sum_{j=1}^{8} w_j\, F_j(T_{DW})\left(U^{-1}V\right)_{ji}\right]}_{A_i} e^{\lambda_i\tau}.\end{aligned} \tag{A.23}$$

Therefore, the PL signal in the 8-level model can be written as a sum of eight exponentials in the dark time:

$$\boxed{\mathrm{PL}(\tau) = \sum_{i=1}^{8} A_i\, e^{\lambda_i\tau},} \tag{A.24}$$

with coefficients

$$\boxed{A_i = k\,\left(V^{-1}\vec{\Psi}\right)_i \sum_{j=1}^{8}\left(\vec{s}^{\,T}\vec{u}_j\right)\, F_j(T_{DW})\,\left(U^{-1}V\right)_{ji}.} \tag{A.25}$$

Equivalently, for any diagonalizable 8-level rate matrix $M = C\Lambda C^{-1}$ with $\Lambda = \mathrm{diag}(\lambda_1, \ldots, \lambda_8)$ and eigenvectors $\vec{C}^{\,i}$ (columns of C), the solution of $\dot{\vec{P}} = M\vec{P}$ is (Berberan-Santos; Martinho, 1990)

$$\vec{P}(t) = e^{Mt}\vec{P}(0) = \sum_{i=1}^{8} \alpha_i\, \vec{C}^{\,i}\, e^{\lambda_i t}, \qquad \alpha_i = \left(C^{-1}\vec{P}(0)\right)_i. \tag{A.26}$$

APPENDIX B – PL Expression - Stretched Exponential Model

First, we define how the number of negatively charged NV centers (denoted by $N^-(t)$) evolves when the laser is turned on and off. Under laser excitation, $N^-(t)$ increases from the initial value N_{in} ($t = 0$) to the maximum number of NV centers, N_{max}, following a stretched exponential function:

$$\mathcal{N}_{on}(N_{in}, t) = \alpha - \beta\, e^{-(a_{bc}t)^m} = \begin{cases} N_{in} = \alpha - \beta, & t = 0, \\ N_{max} = \alpha, & t \to \infty. \end{cases} \tag{B.1}$$

Where $0 < m < 1$. This leads to:

$$\boxed{\mathcal{N}_{on}(N_{in}, t) = N_{max} - (N_{max} - N_{in})\, e^{-(a_{bc}t)^m}}. \tag{B.2}$$

A similar reasoning applies to the dark case, where the number of negatively charged NV centers starts from the value immediately after the laser is turned off, N'_{in}, and reaches the minimum value N_{min} as $\tau \to \infty$:

$$\mathcal{N}_{off}(N'_{in}, \tau) = \alpha' - \beta'\, e^{-(k_{bc}\tau)^n} = \begin{cases} N'_{in} = \alpha' + \beta', & \tau = 0, \\ N_{min} = \alpha', & \tau \to \infty. \end{cases} \tag{B.3}$$

With $0 < n < 1$. This leads to:

$$\boxed{\mathcal{N}_{off}(N'_{in}, \tau) = N_{min} + (N'_{in} - N_{min})\, e^{-(k_{bc}\tau)^n}} \tag{B.4}$$

We now proceed with the calculation for each step of the dark-time experiment, both for the populations and for the number of NV^-. It is important to note that the total number of NV centers is assumed to be constant, i.e., $N^- + N^0 = N_{total}$, where N^0 is the number of NV^0 centers. Additionally, the charge conversion is treated independently from ionization for simplicity.

As discussed in Appendix A, after an initialization pulse of duration t_{init}, the population vector is

$$\vec{\Psi} = e^{M_0\, t_{\text{init}}}\, \vec{P}_0, \quad \text{with } N^-(t_{init}) = N_{max}.$$

We assume that the initialization pulse prepares the system with the maximum number of negatively charged NV centers, N_{max}. In practice, this is not always the case for shorter pulses, which may only polarize the spin into the $m_s = 0$ state; however, this simplification does not affect the final expression.

After the initialization pulse, the system undergoes a dark period of duration τ, during which the populations evolve as

$$\vec{\phi}(\tau) = e^{M_1 \tau}\, \vec{\Psi}.$$

The number of NV^- immediately after the laser is turned off is maximal ($N'_{in} = N_{max}$) and evolves during the dark time as

$$N^-(t_{init} + \tau) = \mathcal{N}_{off}(N_{max}, \tau) = N_{min} + (N_{max} - N_{min})\, e^{-(k_{bc}\tau)^n}. \tag{B.5}$$

Since the photoluminescence detection window coincides with the probing laser, the final population after a probe pulse of duration t is

$$\vec{P}(t, \tau) = e^{M_0 t}\, \vec{\phi}(\tau),$$

and the corresponding number of NV^- centers is

$$N^-(t_{init} + \tau + t) = \mathcal{N}_{on}(N_{in}, t) = N_{max} - (N_{max} - N_{in})\, e^{-(a_{bc}t)^m}, \tag{B.6}$$

where the initial value is $N_{in} = N^-(t_{init} + \tau)$.

Substituting Equation B.5 into Equation B.6, we obtain

$$\begin{aligned} N^-(t_{init} + \tau + t) &= N_{max} - \left[N_{max} - \left(N_{min} + (N_{max} - N_{min})\, e^{-(k_{bc}\tau)^n}\right)\right] e^{-(a_{bc}t)^m} \\ &= N_{max} - (N_{max} - N_{min}) \left[1 - e^{-(k_{bc}\tau)^n}\right]\, e^{-(a_{bc}t)^m}. \end{aligned} \tag{B.7}$$

Defining

$$L(\tau) \equiv (N_{max} - N_{min}) \left[1 - e^{-(k_{bc}\tau)^n}\right], \tag{B.8}$$

the expression can be written in the compact form

$$N^-(t_{init} + \tau + t) = N_{max} - L(\tau)\, e^{-(a_{bc}t)^m}. \tag{B.9}$$

The emission function $R(t, \tau)$ is proportional to the number of emitting NV^-. Assuming that the back-conversion process does not affect the internal electronic dynamics, its effect on the emission can be factorized, leading to

$$\begin{aligned} R(t, \tau) &= N^-(t_{init} + \tau + t)\, k \left[P_3(t, \tau) + P_{4m}(t, \tau) + P_{4p}(t, \tau)\right] \\ &= \left(N_{max} - L(\tau)\, e^{-(a_{bc}t)^m}\right) k \left[P_3(t, \tau) + P_{4m}(t, \tau) + P_{4p}(t, \tau)\right]. \end{aligned} \tag{B.10}$$

In this step it is assumed that an increase of emitting NV^- does not effectively change the other transition rates and any NV-NV interaction is still neglected.

Now, it is possible to substitute this definition of instantaneous emission in the Equation A.17

$$\begin{aligned}\mathrm{PL}_{SE}(\tau) &= \int_0^{T_{DW}} R(t,\tau)\,dt \\ &= k\int_0^{T_{DW}} \left(N_{max} - L(\tau)\,e^{-(a_{bc}t)^m}\right)\vec{s}^{\,T}Ue^{D_0t}U^{-1}\vec{\phi}(\tau)\,dt \\ &= k\int_0^{T_{DW}} \left(N_{max} - L(\tau)\,e^{-(a_{bc}t)^m}\right)\vec{w}^{\,T}e^{D_0t}\vec{\beta}(\tau)\,dt\end{aligned} \tag{B.11}$$

where it was used the definitions in Equation A.18 for the expression of the PL for the stretched exponential model ($\mathrm{PL}_{SE}(\tau)$). We know that the PL expression for the rate-equation only model derived in the previous appendix is given as:

$$PL_{RE}(\tau) = k\int_0^{T_{DW}} \vec{w}^{\,T}e^{D_0t}\vec{\beta}(\tau)\,dt = \sum_{i=1} A_i\,e^{\lambda_i\tau}. \tag{B.12}$$

Conveniently rearranging Equation B.11, we obtain

$$\mathrm{PL}_{SE}(\tau) = N_{max}k\int_0^{T_{DW}} \vec{w}^{\,T}e^{D_0t}\vec{\beta}(\tau)\,dt - L(\tau)\,k\int_0^{T_{DW}} e^{-(a_{bc}t)^m}\vec{w}^{\,T}e^{D_0t}\vec{\beta}(\tau)\,dt, \tag{B.13}$$

To proceed, we consider an approximation for the parameter a_{bc}. The fitted values for k_{bc} and n are $1.32\times10^{-6}\,\mathrm{ns}^{-1}$ and 0.57, respectively. By taking $a_{bc}\sim k_{bc}$, we find that, over the entire detection window $T_{DW} = 1\,\mu s$, the condition $(a_{bc}T_{DW})^n \ll 1$ is satisfied.

Under this condition, the argument of the stretched exponential remains small throughout the integration interval, and the exponential term can be approximated as

$$e^{-(a_{bc}t)^m} \approx 1.$$

Substituting this approximation into Equation B.13, we recover Equation 5.2:

$$\begin{aligned}\mathrm{PL}_{SE}(\tau) &= N_{max}k\int_0^{T_{DW}} \vec{w}^{\,T}e^{D_0t}\vec{\beta}(\tau)\,dt - L(\tau)k\int_0^{T_{DW}} \vec{w}^{\,T}e^{D_0t}\vec{\beta}(\tau)\,dt \\ &= N_{max}PL_{RE}(\tau) - L(\tau)PL_{RE}(\tau) \\ &= (N_{max} - L(\tau))PL_{RE}(\tau) \\ &= \left(N_{max} - (N_{max}-N_{min})\left[1-e^{-(k_{bc}\tau)^n}\right]\right)PL_{RE}(\tau) \\ &= N_{min}\left(1 + \frac{N_{max}-N_{min}}{N_{min}}e^{-(k_{bc}\tau)^n}\right)\sum_{i=1} A_i\,e^{\lambda_i\tau}.\end{aligned} \tag{B.14}$$

This approximation is valid when the characteristic charge conversion time is much longer than the detection window, i.e., $(a_{bc}T_{DW})^n \ll 1$. Therefore, a_{bc} does not need to be strictly equal to k_{bc}; this choice is made for simplicity, as a_{bc} is not the focus of the present analysis. In the simulation it was used $a_{bc} = k_{bc}$.

Experimental data (Figure 18) support this assumption: after a dark time of approximately $10\,\mu s$, a $500\,\mu s$ pulse is still insufficient to saturate the NV^- population, as indicated by the fact that the PL does not reach its maximum value.

Therefore, in this regime of a_{bc}, charge conversion can be considered negligible during the detection process.